Single crystal growth from light, volatile, and reactive materials using lithium and calcium flux.

A. Jesche[1] and P. C. Canfield[1,2]

October 1, 2018

[1] *The Ames Laboratory, Iowa State University, Ames, Iowa, USA*
[2] *Department of Physics and Astronomy, Iowa State University, Ames, Iowa, USA*

Abstract

We present a method for the solution growth of single crystals from reactive Li and Ca melts and its application to the synthesis of several, representative compounds. Among these, single crystalline Li_3N, $Li_2(Li_{1-x}T_x)N$ with $T = \{Mn, Fe, Co\}$, LiCaN, Li_2C_2, LiRh, and LiIr from Li-rich flux as well as Ca_2N, $CaNi_2$, $CaNi_3$, $YbNi_2$, Y_2Ni_7, and $LaNi_5$ from Ca-rich flux could be obtained. Special emphasize is given on the growth of nitrides using commercially available Li_3N and Ca_3N_2 powders as the nitrogen source instead of N_2 gas.

Contents

1 Introduction

Single crystals allow for direct access to the anisotropy of physical properties. Furthermore, the characterization of single crystalline material by means of electric and thermal transport measurements often reflects intrinsic properties to a much higher extent since measurements on polycrystals can be severely affected by grain boundaries, texture, and strain.

For reactive materials there is another advantage: single crystals can be significantly less air-sensitive than polycrystalline or powdered samples due to the formation of a passivating surface layer. This is of great practical value for a basic characterization of magnetic as well as electrical and thermal transport properties. As an example, sample mounting and the transfer of samples from a glovebox to a specific experimental setup, which often provides inert atmosphere during the measurement, is less challenging for reduced air sensitivity and makes experiments with a high throughput of samples much easier. Furthermore, single crystals are often more sustainable and performing experiments after extended periods of storage or shipping is more likely possible than in case of their polycrystalline counterparts.

The first step to successful synthesize compounds containing reactive and volatile materials is finding a suitable container material. Once this is done, we can take advantage of the many benefits of solution growth: reduced reaction temperatures, reduced vapor pressure, work with small amounts of material (compared to using mirror furnaces, Czochralski or Bridgeman methods), and "in-situ purification" of the starting materials often associated with crystallization from the melt.

In this paper, we will demonstrate the use of Li and Ca flux for the single crystal growth of materials containing light, volatile, and reactive materials. Given that both Li and Ca can act as excellent solvents for nitrogen, a special focus will be given to the growth of nitrides.
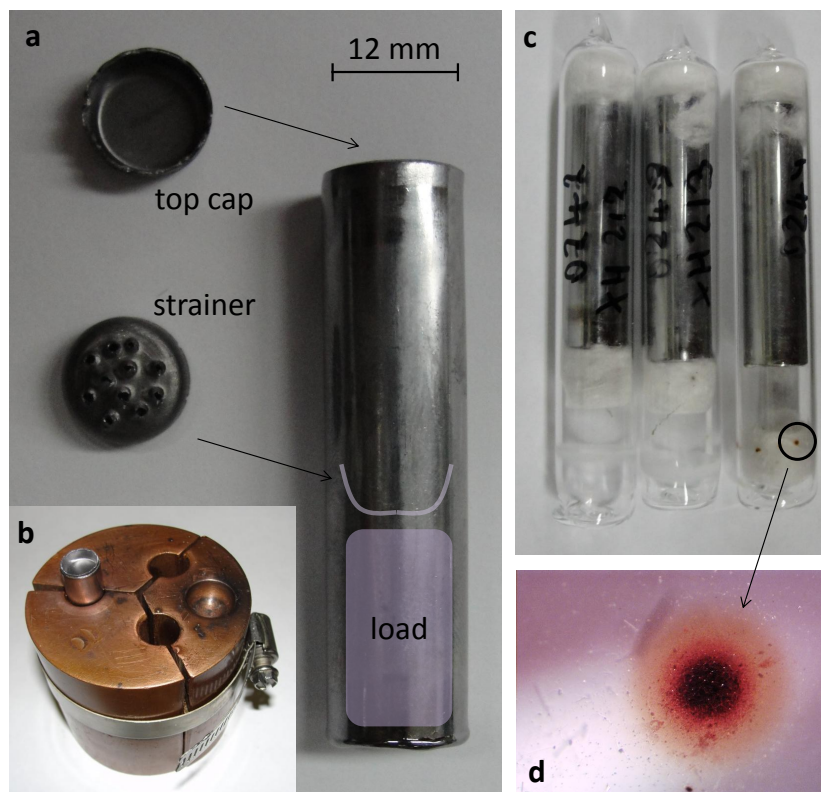
Figure 1: a, Three-cap Ta crucible with top cap and strainer shown separately to left side. b, Massive copper crucible holder for arc welding up to three Ta crucibles in one run. c, Quartz ampules prevent the oxidization of the Ta crucible. The right one shows black-reddish points due to attack. d, Magnified view of such a point which is likely caused by a reaction with Li or Ca which escaped through micro cracks along the welded seam.

2 Experimental methods

Given the reactivity of Li and Ca with silica, we tested Ta and Nb as crucible materials and found both suitable for a variety of compounds and temperature profiles. Ta and Nb, in form of commercially available tubes and sheets, were machined to so called "three-cap crucibles" [1] which allow for easy decanting of excess flux (Fig.1a). A massive copper crucible holder is used to mount the Ta crucibles and provide thermal inertia to keep the elements cool during welding (Fig.1b). One of the caps (bottom) is arc welded into one side of the tube (all arc welding is done under roughly 0.6 atmosphere Ar). After loading the material, a second cap with holes drilled through it is placed above the solid material roughly in the middle of the tube. We found that no further fixation of this cap is necessary provided it fits tightly into the tube. The third cap (top) is arc welded into the top of the tube, sealing the crucible. Care must be taken to prevent a significant heating-up of any volatile materials during this last step. Therefore, the arc welding was performed as quickly as possible and was completed in typically less than one minute. Optical inspection and weighing of the filled crucible before and after arc welding can reveal any signs of vapor transport out of the crucible. Finally, the completed three-cap crucible is sealed in a silica ampule under roughly 1/3 atmosphere Ar to prevent oxidization of Ta or Nb (Fig.1c).

Crystal growth attempts in such three-cap crucibles using Li and Ca flux were performed at temperatures of up to $1200°$ C. After the samples were heated, the silica ampules occasionally showed black-reddish points on the level of the welded seam (Fig.1d). These are likely caused by a reaction with Li or Ca which escaped through micro cracks along the welded seam that might open up only at elevated temperatures. These are still relatively minor leaks and do not significantly hinder crystal growth. This can be contrasted with an actual failure when a faulty sealing resulted in Li substantially attacking the silica ampule. The loss of the silica ampule's integrity lead to a complete disintegration of both Ta crucible and silica ampule and even a surrounding $50\,\mathrm{ml}$ Al_2O_3 support crucible and an underlying hearth plate were damaged. In turn, this sensitivity to larger leaks in the Ta or Nb crucibles, as was demonstrated in this single, failed attempt, shows the general goodness of the sealing obtained in all the other, successful growth attempts.

X-ray diffraction (XRD) was performed using a Rigaku Miniflex diffractometer (wavelength: Cu-$K\alpha_{1,2}$). Part of the measurements were performed under nitrogen atmosphere (see figure captions). Lattice parameters were refined by the LeBail method using GSAS [2] and EXPGUI [3]. Instrument parameter files were determined from measurements on Si and Al_2O_3. XRD powder diffraction measurements on these standard materials have been performed regularly and allow to estimate the relative error for the given lattice parameters to be less than 0.002.

In addition, X-ray diffraction was performed on some of the grown single crystals that show plate-like habit [LiIr, Ca_2N, Y_2Ni_7, and (**Ca**,Y)Ni_3 - see below]. For these measurements, the surface normal, which is parallel to

the crystallographic c-direction, was oriented parallel to the scattering vector. In this way, only $0\,0\,l$ reflections are accessible. Laue-back-reflection patterns were taken with an MWL-110 camera manufactured by Multiwire Laboratories. Magnetization measurements were performed using a Quantum Design Magnetic Property Measurement System (MPMS). Electron microscopy and energy dispersive X-Ray analysis were performed using a JOEL 59101LV system.

3 Lithium flux

With a density of $0.53\,\text{g/cm}^3$ lithium is the lightest solid element at ambient conditions. The low melting temperature of $180°\text{C}$ in combination with a large separation from its boiling temperature ($1342°\text{C}$) fulfill two key characteristics of a good flux. However, the high reactivity and air-sensitivity of lithium requires particular attention. A moderately high vapor pressure ($10^{-2}\,\text{mbar}$ at $520°\text{C}$ [4]) is sufficient to cause a significant attack of silica glass via vapor transport of the Li to the silica. As shown above, sealed Ta crucibles are convenient up to temperatures of $1200°\text{C}$.

Lithium has a low solubility for many transition metals in binary melts, e.g., well below $1\,\text{at.\%}$ for V, Cr, Mn, Fe, Co, Ni at $T = 1000°$ [5]. However, the presence of a third element can increase the solubility significantly. This holds true for low level impurities [5] as well as larger amounts of a third element (see below). A rather good solubility is observed for the noble metals, e.g. for Pd [6] and Pt [7]. A brief review of the growth of intermetallic compounds from lithium flux is given in Ref. [8].

3.1 Nitrides

The high solubility of nitrogen in liquid Li is demonstrated in the binary alloy phase diagram (Fig. 2a after Okamoto [9]). It makes Li a promising flux for nitride single crystal growth at comparatively low temperatures of $800°\text{C}$ and below. Furthermore, other than Li_3N, there are no other Li-N binaries on the Li-rich side that could compete with the formation of other nitrides.

3.1.1 Li_3N

The first step to grow nitrides out of Li-rich flux was to check the suitability of the Ta crucibles in the relevant temperature range and to verify the published binary alloy Li-N phase diagram in the framework of our experiment, in particular to make sure there is not excessive N_2 partial pressure over the melt. This was tested by the syntheses of Li_3N from a $Li_{90}N_{10}$ mixture put together out of Li lumps (Alfa, 99 %) and Li_3N powder (Alfa 99.4 %). The Li-Li_3N mixture was heated from room temperature to $T = 900°\text{C}$ over 5 h, cooled to $T = 750°\text{C}$ within 1.5 h, slowly cooled to $T = 500°\text{C}$ over 50 to 100 h, and finally decanted to separate the Li_3N crystals from the excess liquid. Plate-like single crystals with lateral dimensions limited by the crucible (12 mm) and thickness of up to
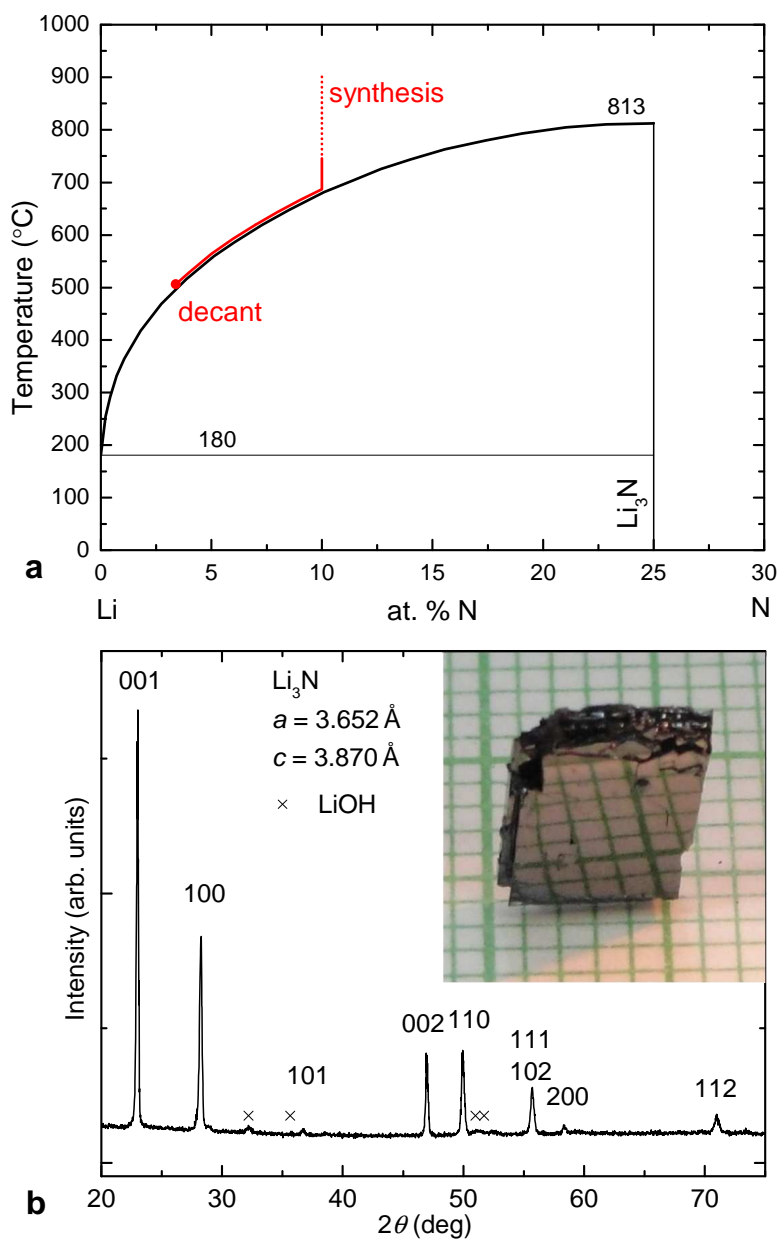
Figure 2: a, Li-N phase diagram after Okamoto [9]. Typical starting composition, temperature profile, and composition of the liquid phase are shown schematically with the red line (the dotted line represents rapid cooling). b, X-Ray powder diffraction pattern measured on ground Li_3N single crystals under nitrogen atmosphere. A representative Li_3N single crystal is shown on a millimeter grid (roughly broken along the sides).

2 mm were obtained. A representative Li_3N single crystal is shown in Fig. 2b on a millimeter grid (roughly broken along the sides perpendicular to the a-b plane). XRD measurements on ground single crystals (Fig. 2b) revealed lattice parameters of $a = 3.652\,Å$ and $c = 3.870\,Å$. This in good agreement with the reported values of $a = 3.648(1)\,Å$ and $c = 3.875(1)\,Å$ [10].

For the $Li_{90}N_{10}$ initial melt composition there was no indication of any significant vapor pressure (as can be inferred from deformation of the Ta crucible). We did find, though, that reducing the Li:N ratio to ∼4:1 (i.e. adding more nitrogen to the melt) and/or heating to temperatures above 1000°C resulted in a significant attack of the Ta crucibles which became very brittle even though no leaks occurred. In contrast, the Ta crucibles remained metallic, flexible and showed no signs of attack when using temperature profile and melt compositions as described above.

3.1.2 $Li_2(Li_{1-x}T_x)N$ with $T = $ Mn, Fe, Co

Transition metals (T) can be incorporated in Li_3N where they occupy only one of the two the Li sites (the $1b$ Wyckoff site which is two fold coordinated by nitrogen)[11]. However, it is surprising that we were able to grow single crystals containing significant amounts of transition metals (e.g. $x = 0.28$ for Fe) despite their reported negligible solubility in Li. The formation of T-N or T-N-Li complexes in the liquid state apparently allow much more transition metal to be incorporated into the Li-rich flux.

Extensive work has been performed on the $Li_2(Li_{1-x}Fe_x)N$ series which shows an extreme magnetic anisotropy and coercivity as well as exotic tunneling effects of the magnetization [12]. An important aspect is the absence of ferromagnetic or superparamagnetic Fe particles as shown by magnetization measurements [12]. This would be difficult to achieve using alternative growth procedures. The starting materials were mixed in a molar ratio of $Li:Fe:Li_3N = 6$-x_0:x_0:1 with x_0 ranging from 0 to 0.5 (corresponding to a melt stoichiometry of $Li_{85}Fe_5N_{10}$ for the latter one). The mixtures with a total mass of roughly 1.3 g were packed in a three-cap Ta crucible, heated from room temperature to $T = 900°C$ over 5 h, cooled to T = 750°C within 1.5 h, slowly cooled to 500°C over 60 to 100 h, and finally decanted to separate the single crystals from the excess flux. For slow cooling rates the sample size was limited by the crucible. The crystal habit for $T = $ Fe is similar to undoped Li_3N single crystals for the whole concentration range ($x = 0.00013 - 0.28$). Notice that even nominally undoped Li_3N shows Fe concentrations of $x = 0.0001$ to 0.0003 that originate from Fe impurities in either the starting materials or leached from the Ta crucibles [12]. As demonstrated in Figs. 3a,b and observed in several additional growth procedures there is little change in the crystal habit as Fe is incorporated in the melt.

In contrast, the crystal habit for $T = $ Mn and Co differs significantly from undoped Li_3N (Fig. 3c). The growth parameters were the same as for the growth of undoped Li_3N single crystal shown in Fig. 3a. Doping levels of as little as $x_0 = 0.03$ Mn or Co, corresponding to 0.3 at.% in the melt, lead to significant
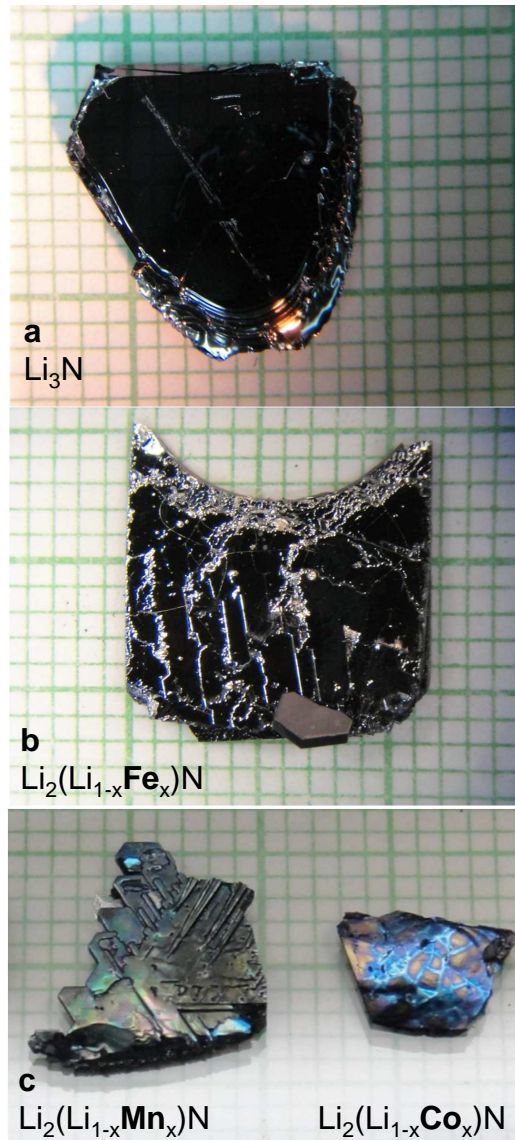
Figure 3: As-grown single crystals of nominally pure and doped Li_3N on a millimeter grid. a, Nominally pure Li_3N single crystal (actual composition being $\sim Li_{2.9999}Fe_{0.0001}N$ - see text) obtained by slowly cooling a $Li_{90}N_{10}$ mixture from $750°C$ over $67\,h$ to $550°C$. b, $Li_2(Li_{1-x}Fe_x)N$ single crystal decanted at a lower temperature of $T = 500°C$ showing a crucible-limited size. The $Li_{89}Fe_1N_{10}$ mixture was slowly cooled from $750°C$ over $63\,h$ to $500°C$ resulting in $x \sim 0.1$. Doping Fe has no significant effect on the crystal habit when compared to nominally undoped Li_3N. c, In contrast, adding as little as $0.3\,at.\%$ Mn or Co to the melt changes the crystal habit significantly (the temperature profile used in these cases was identical to the one of nominally pure Li_3N shown above).

changes in size, aspect ratio and formation of facets. For $T = $ Mn much clearer hexagonal, edge faceting is apparent. For $T = $ Co, the single crystals were smaller and significantly thinner ($\sim 0.05\,\text{mm}$) when compared with undoped Li_3N or $T = $ Fe. Magnetization measurements confirm the presence of Mn and Co.

Attempts to grow $Li_2(Li_{1-x}T_x)N$ for $T = $ Sc, Ti, V, Cr failed. The product consisted of undoped Li_3N and, partially, the unreacted transition metals were still visible with the shape of the starting material preserved. To our knowledge, an oxidation state of predominantly +1 is not observed for Sc, Ti, V, or Cr in solids and this may be the origin for the failure of substituting Li by these elements. This can be viewed as being consistent with the idea of an oxidation state of +1 for $T = $ Mn, Fe, Co in these compounds which, although unusual, is reasonable for replacing Li^{+1}. For $T = $ Cu and Ni this has been demonstrated by X-ray absorption spectroscopy [13].

A negative aspect of the surprising solubility of some transition metals in the $Li_{90}N_{10}$ melt is the possibility of also increasing the solubility of Ta or Nb in Li which is basically zero in the absence of nitrogen. This may be partially responsible for the change of the crucible materials as observed at higher temperatures.

3.1.3 AlN

Polycrystalline AlN was obtained as a result of an attempt to grow either AlN or $AlLi_3N_2$ from a Li-rich flux. The formation of AlN from elemental Al dissolved in a $Li_{94}N_6$ melt is an important result since it proves that the Li_3N binary compound is not so stable that it prevents the growth of other (Li-free) nitrides. It is reasonable to assume that this is not restricted to Al and that Li flux can be used as an exploratory tool for the growth of novel nitrides as well as for the growth of large single crystals of known compounds.

The starting materials were mixed in a molar ratios of $Li:Al:Li_3N = 10:2:2$ (corresponding to $Li_{71}Al_{14}N_{14}$). The mixture with a total mass of roughly $1.5\,\text{g}$ was packed in a three-cap Ta crucible, heated from room temperature to $T = 900^\circ\text{C}$ over $4\,\text{h}$, slowly cooled to 400°C over $44\,\text{h}$, and finally decanted. Polycrystalline AlN was found at the bottom of the Ta crucible. Specular reflecting facets of $\sim 50\,\mu\text{m}$ along a side were observed among the polycrystalline material. These are likely attributed to small AlN single crystals suggesting that even more diluted melts, along with slower cooling might be needed for growth of larger AlN grains.

Powder XRD measurements on AlN (Fig. 4) revealed lattice parameters of $a = 3.116\,\text{Å}$ and $c = 4.986\,\text{Å}$. This in good agreement with the reported values of $a = 3.1115\,\text{Å}$ and $c = 4.9798\,\text{Å}$ [14].

3.1.4 LiCaN

Initially, we observed LiCaN as a by-product of the growth of Li_3N where Ca was introduced as an impurity phase of the starting materials (Alfa, Li lumps 99 %,
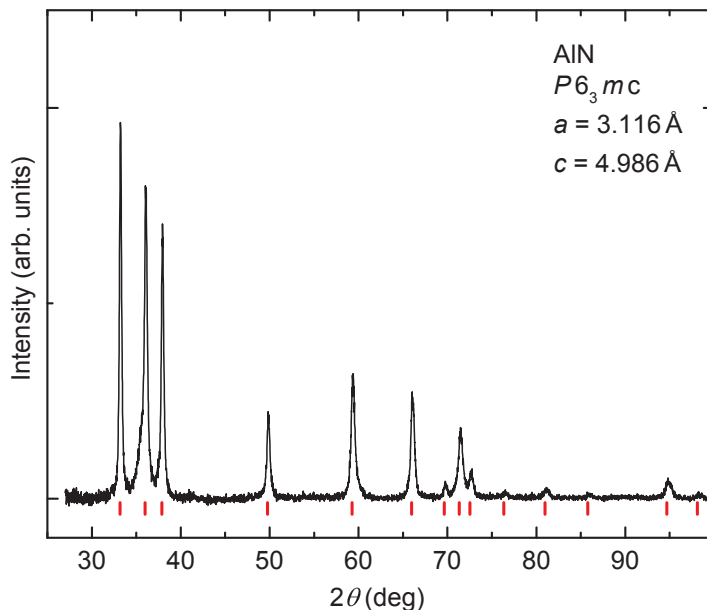
Figure 4: X-Ray powder diffraction pattern collected under nitrogen atmosphere. The theoretical peak positions are marked by red bars.

Li$_3$N powder 99.4 %). The amount of LiCaN can be estimated to less than 1 % of the growth product, consistent with the purity of the starting materials. Later, we added Ca intentionally to the melt in order to grow larger quantities of this material. The starting materials were mixed in a molar ratio of Li:Ca:Li$_3$N = 6:1:1 (corresponding to Li$_{82}$Ca$_9$N$_9$). The mixture with a total mass of roughly 1.4 g was packed in a three-cap Ta crucible, heated from room temperature to $T = 900°$C over 4.5 h, cooled to T = 750°C within 1.5 h, slowly cooled to 350°C over 90 h, and finally decanted to separate the LiCaN crystals from the remaining liquid.

Rod-shaped single crystals with lengths of up to 5 mm and cross-sectional dimensions of up to 1 mm were obtained (Fig.5a). The orange color is clearly visible in crushed single crystals (upper, left inset in Fig.5a) whereas the color of the as grown samples often appears more faint due to flux remnants on the sample surface. A LiCaN single grown as a by-product from a nominally Ca-free Li$_{90}$N$_{10}$ solution, i.e. a very dilute Li$_{90-\delta}$Ca$_\delta$N$_{10}$ solution, is shown in the lower, right inset of Fig.5a. The surface is cleaner and the orange color more apparent when compared to the samples grown from a more Ca-rich flux.

Powder XRD measurements on ground LiCaN single crystals (Fig. 5b) revealed lattice parameters of $a = 8.493$ Å, $b = 3.682$ Å and $c = 5.550$ Å. The reported values of $a = 8.471(3)$ Å, $b = 3.676(2)$ Å and $c = 5.537(3)$ Å are somewhat smaller [15]. These values were obtained by means of single crystal diffraction on samples grown from a Li$_6$Ca mixture under nitrogen atmosphere. Fur-
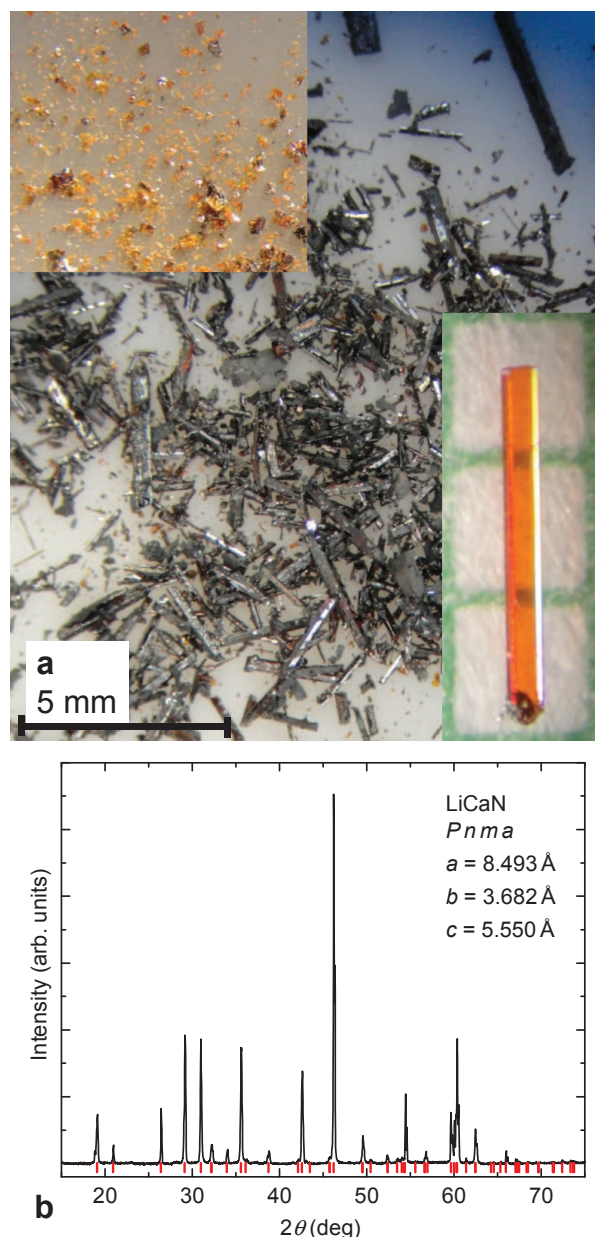
Figure 5: a, Single crystals of LiCaN grown from a $Li_{82}Ca_9N_9$ melt, partially coated with grayish flux remnants. The orange color becomes apparent after breaking or grinding the samples (upper left part). An as-grown LiCaN single crystal obtained as a by-product from a $Li_{90}N_{10}$ melt is shown on a millimeter grid (lower right part, Ca was introduced as an impurity - see text). b, X-Ray powder diffraction pattern collected under nitrogen atmosphere. The theoretical peak positions are marked by red bars.

thermore, a plate-like habit is reported [15] whereas we observe a pronounced rod-like habit. The cause of the observed differences is unclear so far.

3.2 Non-nitrides

In addition to its ability to bring nitrogen into a useful solution, Li can act as a solvent for other elements as well. In this section we present proof of principle growths for a representative selection of other binary melts.

3.2.1 Li_2C_2

In order to evaluate the feasibility of a Li-rich flux for the growth of carbides we grew Li_2C_2 out of a binary melt. As described above for the case of Li_3N, the following key questions had to be answered: is the Ta-crucible attacked, is the solubility sufficient, does the crystallization take place in a controlled fashion? Informally the question is, "Can we get carbon IN and OUT of solution?" The growth of Li_2C_2 single crystals of roughly one millimeter along a side provides a positive answer to all of these questions.

The starting materials were mixed in a molar ratio of Li:C = 9:1. The mixture with a total mass of roughly 0.8 g was packed in a three-cap Ta crucible, heated from room temperature to $T = 1000°C$ over 5 h, held for 1 h, slowly cooled to 400°C over 60 h, and finally decanted to separate the Li_2C_2 crystals from the excess liquid. The product is air-sensitive in powder form and decays on a timescale of one day. XRD measurements on ground Li_2C_2 single crystals (Fig. 6c) revealed lattice parameters of $a = 3.656$ Å, $b = 4.834$ Å and $c = 5.442$ Å. This in good agreement with the reported values of $a = 3.655$ Å, $b = 4.830$ Å, $c = 5.440$ Å [16] and $a = 3.6520(1)$ Å, $b = 4.8312(2)$ Å, $c = 5.4344(1)$ Å [17].

3.2.2 Li_3Al_2

The Li-Al binary phase diagram contains two Li-rich line compounds: Li_3Al_2 and Li_9Al_4 [18]. In order to test the viability of the Li-Al melt we grew Li_3Al_2. An attempt to grow single crystals from a $Li_{80}Al_{20}$ mixture yielded dendritic structures at the bottom of the Ta crucible (Fig. 7). The mixture with a total mass of roughly 1.1 g was packed in a three-cap Ta crucible, heated from room temperature to $T = 600°C$ over 3 h, held for 2 h, slowly cooled to 360°C over 60 h, and finally decanted.

XRD measurements on ground Li_3Al_2 dendrites (Fig. 7) revealed lattice parameters of $a = 4.482$ Å and $c = 14.18$ Å. This is somewhat smaller than the reported values of $a = 4.508(7)$ Å and $c = 14.259$ Å [19]. Magnetization measurements on a cluster of Li_3Al_2 dendrites revealed a roughly temperature-independent diamagnetic susceptibility of $-2.4(2) \cdot 10^{-10}$ $m^3 mol^{-1}$ for $T = 50$ to 300 K (Fig. 8, measured in an applied magnetic field of $\mu_0 H = 7$ T). An increase of the susceptibility upon cooling below ~ 50 K (Curie tail) can be attributed to a small amount of local moment bearing magnetic impurities. No indications for phase transitions were observed. In particular, additional
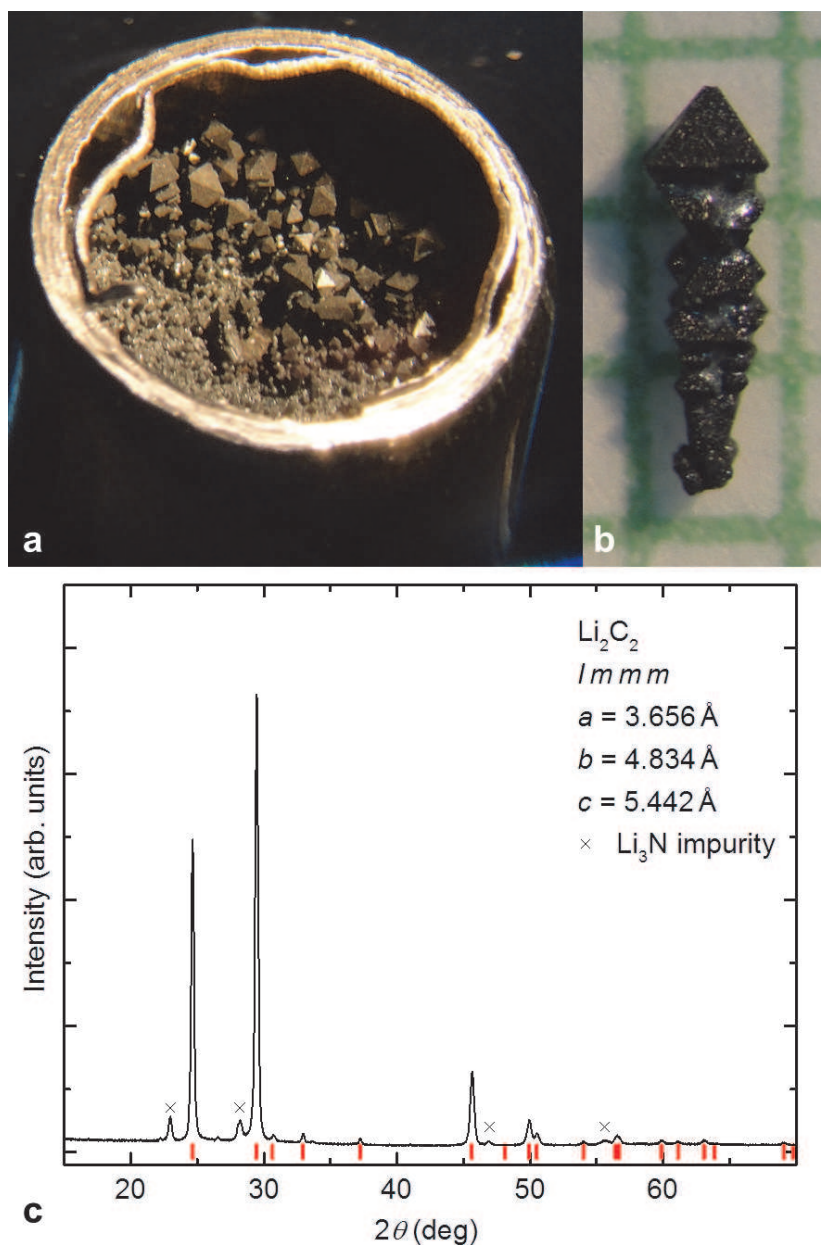
Figure 6: a, Li_2C_2 single crystals in the opened bottom part of a three-cap Ta crucible. b, An isolated crystal is shown on a millimeter grid. c, X-Ray powder diffraction pattern collected under nitrogen atmosphere. The theoretical peak positions are marked by red bars. The Li_3N impurity likely originates from Li-rich flux remnants which were attached to the Li_2C_2 single crystals (see silver-grey droplets in b) that decay to Li_3N under the nitrogen atmosphere surrounding the X-Ray system.
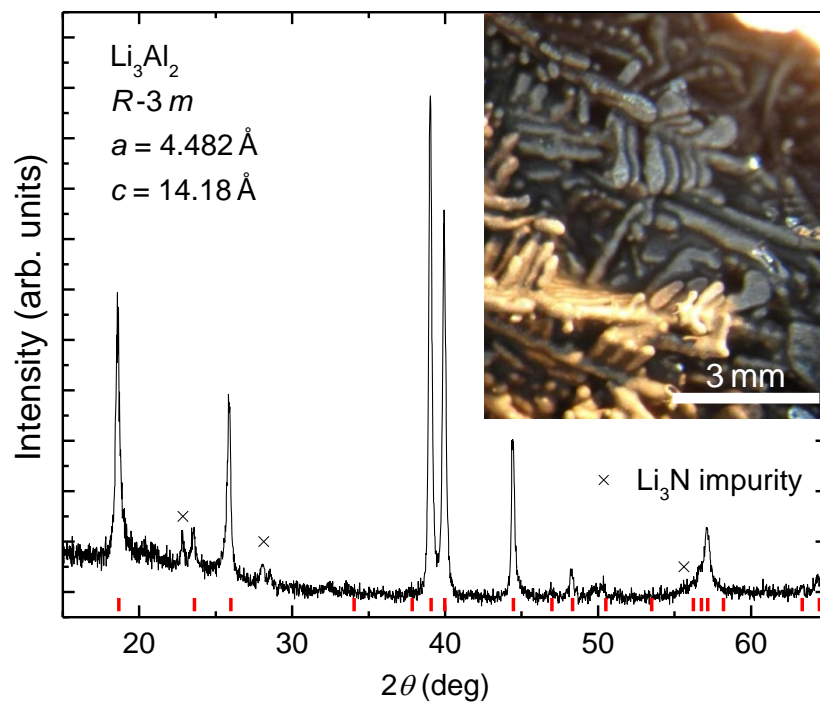
13

Figure 7: X-Ray powder diffraction pattern collected under nitrogen atmosphere. The theoretical peak positions for Li_3Al_2 are marked by red bars. A small amount of a Li_3N impurity phase likely stems from Li-rich flux remnants which decay to Li_3N under nitrogen atmosphere. The inset shows Li_3Al_2 dendrites grown from Li-rich flux.
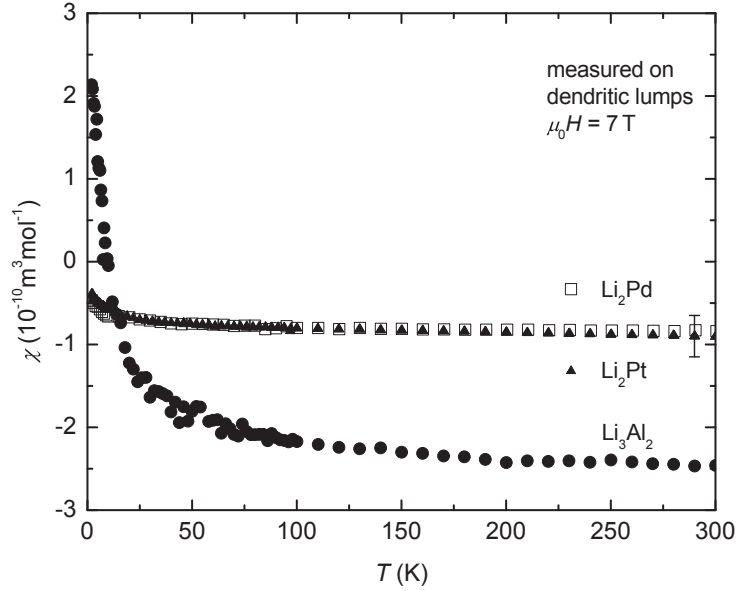
Figure 8: Temperature dependent magnetic susceptibility, $\chi = M/H$, of Li_3Al_2, Li_2Pd, and Li_2Pt. The compounds are diamagnetic with a roughly temperature-independent susceptibility for $T = 50$ to $300\,K$. The upturn observed upon cooling below $\sim 50\,K$, more pronounced for Li_3Al_2, is attributed to a small amount of a local moment bearing impurity. The estimated error is shown, for example, for Li_2Pt at $T = 290\,K$).

measurements performed in small applied fields revealed no signs of superconductivity for $T_c > 2\,K$.

3.2.3 Li_2Pd and Li_2Pt

In order to test the solubility of Pd and Pt in Li as well as our ability to contain Li-Pd and Li-Pt melts we chose Li_2Pd and Li_2Pt as target materials. They required moderate Pd and Pt concentrations as well as temperatures up to $\sim 1000°C$. Our attempts to grow Li_2Pd and Li_2Pt single crystals from a Li-rich flux yielded phase clean material showing pronounced dendritic structures (Fig. 9).

The starting materials for Li-Pd were mixed in a molar ratio of Li:Pd = 70:30 and Li:Pd = 73:27. The mixtures with a total mass of roughly 4 g were packed in three-cap Ta crucibles, heated from room temperature to $T = 1000°C$ over 5 h, held for 0.5 h, cooled to 610°C over 4 h, slowly cooled to 410°C over 40 h, and finally decanted. The starting materials for Li-Pt were mixed in a molar ratio of Li:Pt = 77:23 and Li:Pt = 80:20. The mixtures with a total mass of roughly 4 g were packed in three-cap Ta crucibles, heated from room
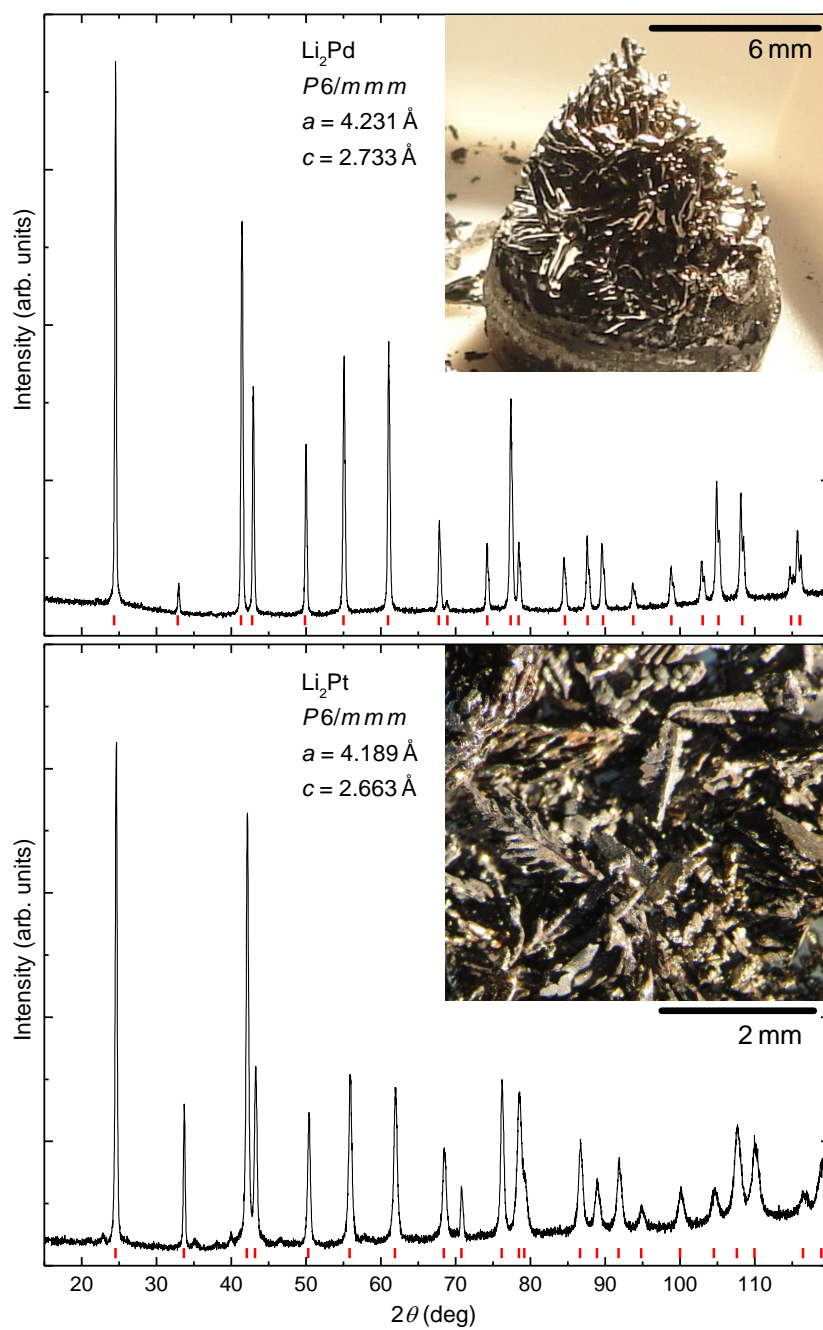
Figure 9: X-Ray powder diffraction pattern of Li_2Pd and Li_2Pt collected under nitrogen atmosphere. The theoretical peak positions are marked by red bars. The insets show the pronounced dendritic structures as observed for both compounds.

16

temperature to $T = 1000°C$ over $5\,\mathrm{h}$, held for $2\,\mathrm{h}$, cooled to $800°C$ over $2\,\mathrm{h}$, slowly cooled to $350°C$ over $55\,\mathrm{h}$, and finally decanted. Slower cooling or use of powdered Pd and Pt or pre-arc-melted lumps of Pd and Pt had no significant effect on the growth result.

XRD measurements on as-grown dendrites of Li_2Pd (Fig. 9) revealed lattice parameters of $a = 4.231\,\text{Å}$, and $c = 2.733\,\text{Å}$. Rather surprisingly, the measured intensities show no signs of a preferred orientation. A measurement on ground dendrites revealed the same result. The obtained lattice parameters are in good agreement with the reported values of $a = 4.2267\,\text{Å}$ and $c = 2.7319\,\text{Å}$ [20]. XRD measurements on ground dendrites of Li_2Pt (Fig. 9) revealed lattice parameters of $a = 4.189\,\text{Å}$, and $c = 2.663\,\text{Å}$. This is significantly smaller than the values obtained for Li_2Pd and in good agreement with the literature data of $a = 4.186\,\text{Å}$, and $c = 2.661\,\text{Å}$ [21].

Recent band-structure calculations propose that the Pt atoms in Li_2Pt exist as partially negative anions [22] which is unusual for transition metals. However, this compound is, similar to isoelectronic Li_2Pd, rarely investigated experimentally. Magnetization measurements performed on dendritic lumps revealed a roughly temperature-independent diamagnetic susceptibility of $-0.9(2) \cdot 10^{-10}\,\mathrm{m^3}$ $\mathrm{mol^{-1}}$ for both Li_2Pd and Li_2Pt (Fig. 8). A small increase of the susceptibility upon cooling below $\sim 50\,\mathrm{K}$ (Curie tail) can be attributed to a small amount of local-moment bearing magnetic impurities. No indications for phase transitions were observed. In particular, additional measurements performed in small applied fields revealed no signs of superconductivity down to $2\,\mathrm{K}$.

3.2.4   LiRh and LiIr

The published binary alloy phase diagrams for Li-Rh and Li-Ir indicate an uncertainty of the liquidus temperatures ('The assessed Li-Rh phase diagram is highly speculative' [23]). In order to get a rough sense on how well Rh and Ir dissolve in Li we performed attempts to grow LiRh and LiIr from a Li-rich flux. The starting materials for Li-Rh and Li-Ir were mixed in a molar ratio of Li:Rh/Ir = 95:5. Rh and Ir were arc melted prior to the growth in order to reduce the amount of hydrogen and other volatile impurities and provide recognizable lumps in the case of poor or no solubility. The mixtures with a total mass of roughly $1.5\,\mathrm{g}$ were packed in three-cap Ta crucibles, heated from room temperature to $T = 1000°C$ over $5\,\mathrm{h}$, held at $1000°C$ for $1\,\mathrm{h}$, cooled to $900°C$ over $2\,\mathrm{h}$, slowly cooled to $250°C$ over $90\,\mathrm{h}$, and finally decanted to separate the single crystals from the excess liquid. We succeeded in growing plate-like single crystals of LiRh with lateral dimensions of up to $2\,\mathrm{mm}$ and thickness of $\sim 0.5\,\mathrm{mm}$ using a Li-rich flux (Fig. 10a). The analogous attempt to grow LiIr yielded smaller single crystals up to $0.25\,\mathrm{mm}$ along a side with a thickness of $\sim 20\mu\mathrm{m}$ (Fig. 10b). The significantly smaller size of the LiIr single crystals indicates differences in the nucleation and growth process when compared to LiRh. A possible reason is a higher liquidus temperature for $Li_{95}Ir_5$ in close vicinity to the maximum furnace temperature of $1000°C$. This scenario would be consistent with the melting temperature of LiIr being roughly $200°C$ higher than the one

LiRh

LiIr

a

b

Intensity (arb. units)

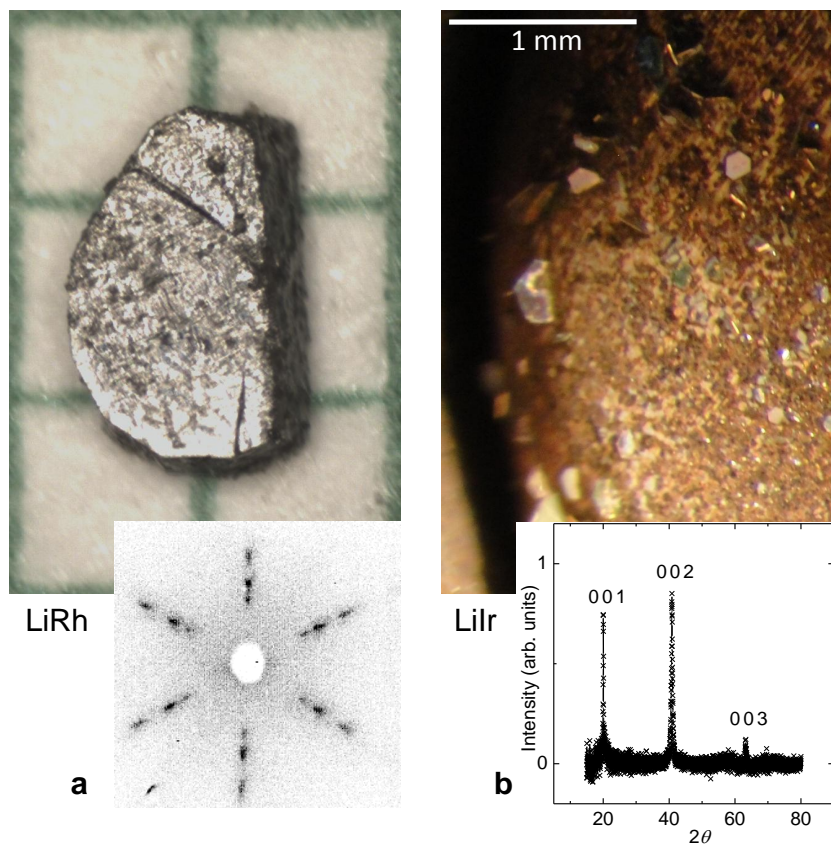0 0 1

0 0 2

0 0 3

1 mm

2θ

20   40   60   80

Figure 10: a, Single crystal of LiRh on a millimeter grid and corresponding Laue-back-reflection pattern. b, LiIr single crystals attached to the bottom of a Ta crucible. The X-Ray diffraction pattern was recorded (in air) on a single crystal with the surface normal of the plate-like sample parallel to the scattering vector.

of LiRh [23]. Another very different possibility is a eutectic point in the vicinity of $\sim$Li$_{96}$Ir$_4$ (which is shifted to a higher Li concentration for LiRh).

The crystal structure of LiRh was studied by means of X-ray and neutron diffraction (space group $P\,\bar{6}$ originally reported [24], later revised to $P\,\bar{6}\,m\,2$ [25]). The synthesis and crystal structure of LiIr was reported in 1976 [26] (isostructural to LiRh). Furthermore, both the Li-Rh-H [27] and the Li-Ir-H [28] system were investigated. Besides these early studies we are not aware of any report on physical properties of these rather simple binaries. The sixfold crystallographic c-axis is oriented perpendicular to the larger surface of the plates as confirmed by Laue-back-reflection for LiRh and for LiIr by X-ray diffraction in a (symmetric) θ-2θ geometry on oriented plates (the scattering vector is parallel to surface normal, the sample size of the LiIr single crystals is not sufficient for the available Laue-back-reflection setup). Both, the LiRh and the LiIr single crystals were found to be extremely malleable. Accordingly, we did not succeed in grinding the material to a powder suitable for X-ray diffraction. However, a powder diffraction pattern of LiIr could be obtained from polycrystalline material which got stuck at the strainer of the used Ta crucible (not shown). The determined lattice parameters of $a = 2.650\,\text{Å}$ and $c = 4.399\,\text{Å}$ are in good agreement with the reported values [$a = 2.650(1)$ Å and $c = 4.398(2)$ Å [26]].

A basic characterization of LiRh by means of temperature-dependent electrical resistivity, magnetization and specific heat is presented in Fig. 11. No indications for phase transitions were observed for $T = 2$ to $300\,\text{K}$. The electrical resistivity shows the temperature-dependence of a normal metal with a residual resistivity ratio of RRR $= 5$ and a residual resistivity of $\rho_0 = 1.5\,\mu\Omega\,\text{cm}$ (Fig. 11a). The low-temperature specific heat reveals a slightly enhanced Sommerfeld coefficient of $\gamma = 7.2\text{mJ}\,\text{mol}^{-1}\,\text{K}^{-2}$ (Fig. 11b). The Debye temperature is estimated to $\Theta_\text{D} = 182\,\text{K}$ (low temperature limit). This rather small value is in accordance with the observation of small Debye temperatures in soft materials whereas hard materials show higher values (see e.g. [29]). Temperature-dependent and isothermal magnetization show the typical behavior of a paramagnetic metal (Figs. 11c,d).
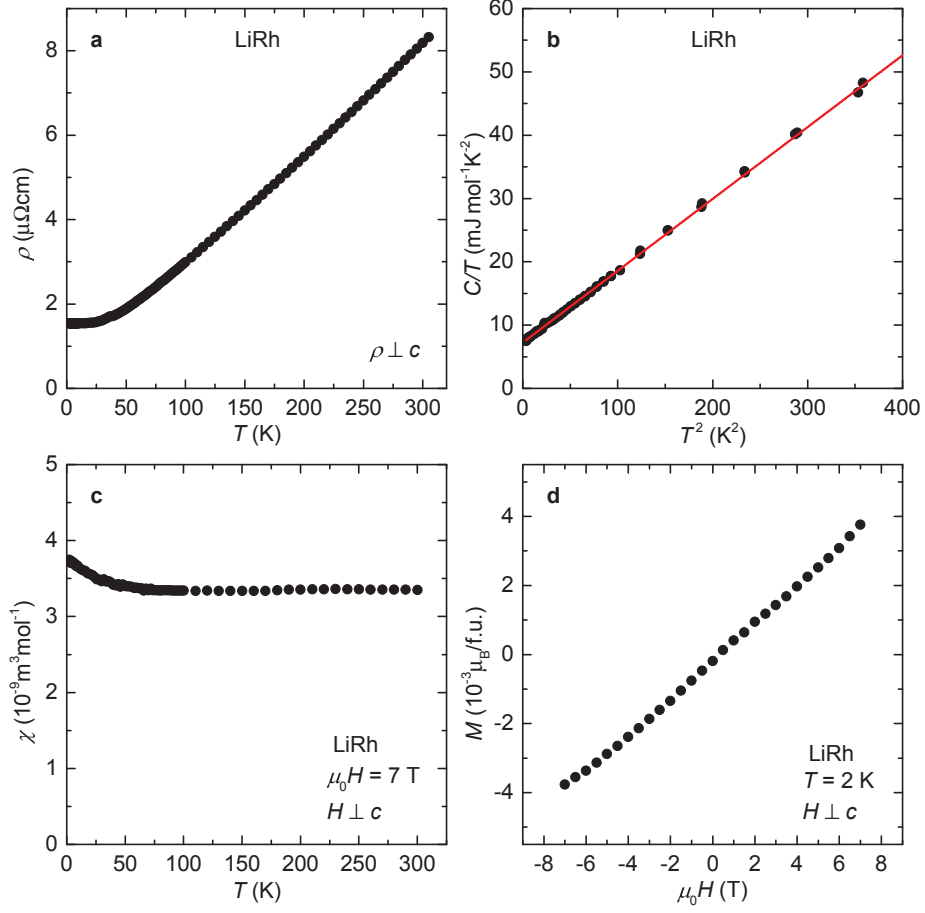
Figure 11: Basic properties of LiRh. Temperature-dependent electrical resistivity (a), specific heat (b), and magnetization (c) as well as isothermal magnetization (d) indicate a magnetically non-ordered, metallic state for $T = 2$ to 300 K.
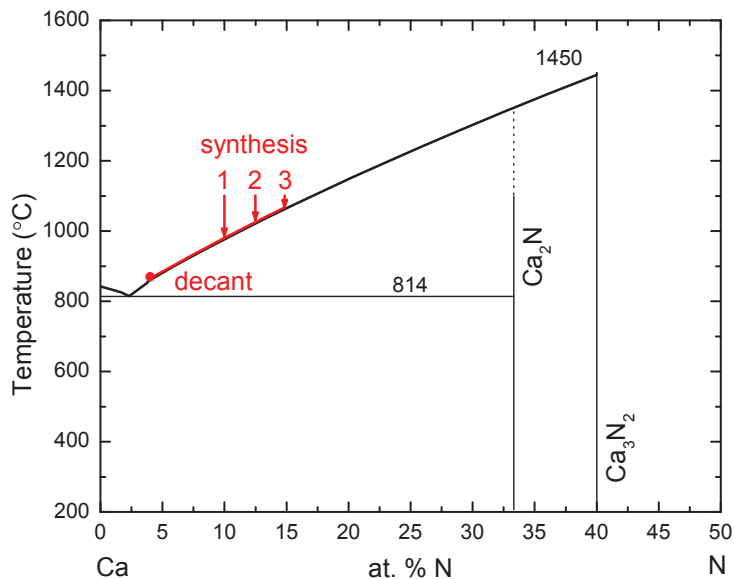
Figure 12: Revised Ca-N phase diagram based on [31, 32]. The starting compositions (1, 2, and 3) and temperature profile are shown with the red line. Transformations between Ca_2N, Ca_3N_2, and β-Ca_3N_2 (not shown) depend on temperature and (nitrogen) pressure as reported by Höhn *et al.* [32].

4   Calcium flux

With a density of $\rho = 1.55\,\text{g/cm}^3$ calcium is the lightest of the alkaline earth elements. It is highly reactive and air and moisture sensitive. This, as well as the moderately high melting temperature of $842°\text{C}$ and vapor pressure of $2\,\text{mbar}$ at $T = 842°\text{C}$ [4] makes crystal growth from calcium flux a challenging task. Promising, on the other hand, is the excellent solubility for the light elements N, C, and Al and further for the transition metals Ni, Cu, Pd, Ag, Pt, and Au in Ca (e.g. [30]).

In section 4.1 we present results on the single crystal growth of binary calcium nitrides from Ca-rich melts. Several attempts to grow other nitrides from Ca-N-X ternary melts failed, presumably due to the relatively high stability of binary Ca_2N. A brief report on these attempts, including CaNiN, $CaMg_2N_2$, Ca_3AuN, $Ag_{16}Ca_6N$, and $Ag_8Ca_{19}N_7$ is presented in section 5. Section 4.2 summarizes our uses of Ca to bring Ni into solution and grow Ca-Ni binary compounds as well as representative R-Ni compounds (R = Y, La, Yb). As such, we believe that, in addition to its use as a solvent for light and reactive elements, Ca-rich flux is a suitable exploratory tool for the synthesis of rare earth bearing compounds at comparatively low temperatures.
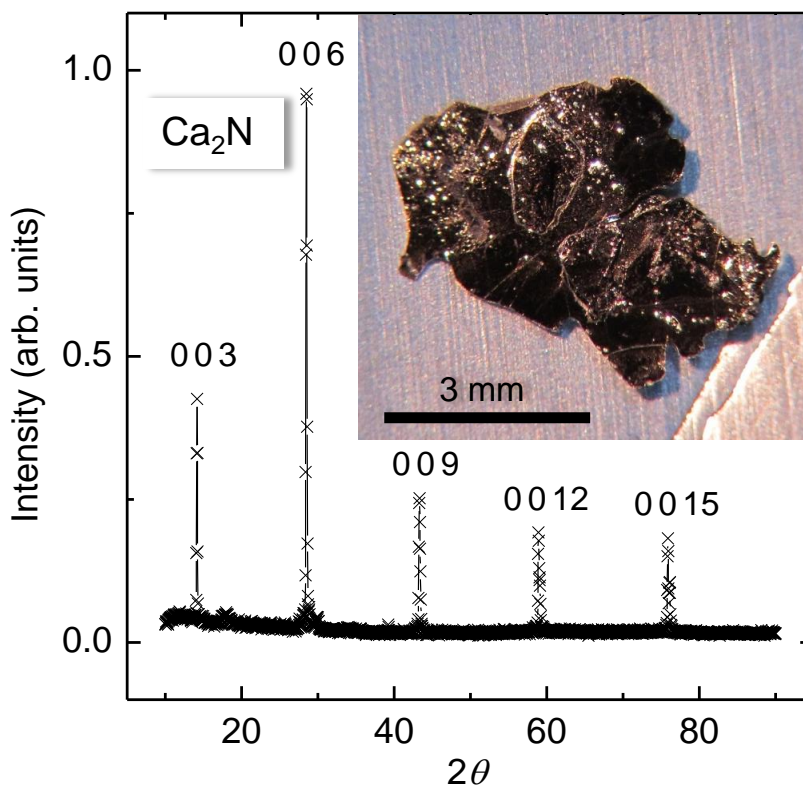
Figure 13: Single crystal of Ca_2N with a thickness of $\approx 50\,\mu m$ obtained from a $Ca_{85}N_{15}$ melt. The X-Ray diffraction pattern was recorded under nitrogen atmosphere on a single crystal with the surface normal of the plate-like sample parallel to the scattering vector.

4.1 Ca_3N_2 and the subnitride Ca_2N

The high solubility of nitrogen in liquid Ca is demonstrated in the binary alloy phase diagrams (Fig. 12 after [31]). The phase transformations between Ca_2N, Ca_3N_2, and a third binary, β-Ca_3N_2 (not shown in Fig. 12), are reported to depend on temperature and (nitrogen) pressure [32]. It should be noted that Ca_2N is not included in the early binary phase diagram [31]. In full analogy to the nitride growth from Li-rich flux described in the previous section, the first step to grow nitrides out of a Ca-rich flux was an attempt to grow either Ca_3N_2 or Ca_2N single crystals.

The starting materials used were Ca and Ca_3N_2. They were mixed in molar ratios of 15:1, 11:1, and 25:3 so as to give initial melt stoichiometries of $Ca_{90}N_{10}$, $Ca_{87.5}N_{12.5}$, and $Ca_{85}N_{15}$, respectively. The mixtures, each with a total mass of roughly 2.5 g, were packed in a three-cap Ta and Nb crucibles, heated from room temperature to $T = 1100°C$ over 5.5 h, slowly cooled to $880°C$ over 38

to 122 h, and finally decanted to separate the single crystals from the excess flux. The Nb crucibles were found to be better than Ta crucibles which became brittle at temperatures above $1000°C$ and/or high N concentrations.

We obtained thin, plate-like single crystals of Ca_2N with lateral dimensions of up to 5 mm and thickness of typically $50\,\mu m$ (Fig. 13). The initial composition of the melt had only minor effects on the phase formation and crystallization. Only a small tendency towards larger and thicker Ca_2N single crystals was found for $Ca:Ca_3N_2 = 25:3 \equiv Ca_{85}N_{15}$. No traces of the starting material Ca_3N_2 were found. From these data we can infer that there is primary solidification of Ca_2N for each of these melts with the liquidus line existing below $1100°C$, even for $Ca_{85}N_{15}$.

Ca_2N is highly air-sensitive [33] and the single crystals grown from Ca-rich flux show the formation of a white-colored surface layer within a few minutes on air. However, it takes several hours for the samples to completely decompose indicating that the surface layer is passivating to a certain degree. The Ca_2N single crystals are too malleable to grind them into a fine powder. Therefore, X-Ray diffraction was performed on single crystals with the surface normal of the plate-like samples parallel to the scattering vector. The main peaks in the diffraction pattern (Fig. 13) can be indexed based on $0\,0\,3l$ reflections as expected for Ca_2N (according to the reflection conditions for space group $R\bar{3}mf$ with hexagonal axes).

The electrical resistance of Ca_2N at room temperature was estimated using a standard multimeter in an Ar filled glove box. Contacting the single crystals with two tungsten needles, which were gently stuck into the sample, revealed an electrical resistance too small to be quantified (less than $1\,\Omega$ corresponding to a resistivity of a few mΩcm). However, several attempts to contact samples in four point geometry using silver paint, silver epoxy or carbon paste led to contact resistances of several hundred Ohms and above. Curing the contacts or reducing the contact resistance by annealing or applying electric currents failed (the samples were always handled in Ar or nitrogen filled glove boxes). An extreme sensitivity to solvents present in standard contact pastes might be at the origin of the enhanced resistance. For polycrystalline Ca_2N differing values of $\rho = 0.16\,\Omega\text{cm}$ [32] and $\rho = 63\,\Omega\text{cm}$ [33] were reported (measured at room temperature). It is reasonable to assume that the electrical transport of this '2D "excess electron" compound' [33] is highly anisotropic. A further optimization of the growth procedure and the development of suitable electric contacts may be necessary to study the electric transport in detail and to evaluate possible similarities to other 2 dimensional electron systems like graphene.

4.2 Non-nitrides

4.2.1 CaNi$_2$ and CaNi$_3$

Single crystals of $CaNi_2$ and $CaNi_3$ with dimensions of several millimeters were grown from a Ca-rich self-flux (Fig. 15). Both compounds were found to be metals in close vicinity to a ferromagnetic instability. $CaNi_2$ crystallizes in the
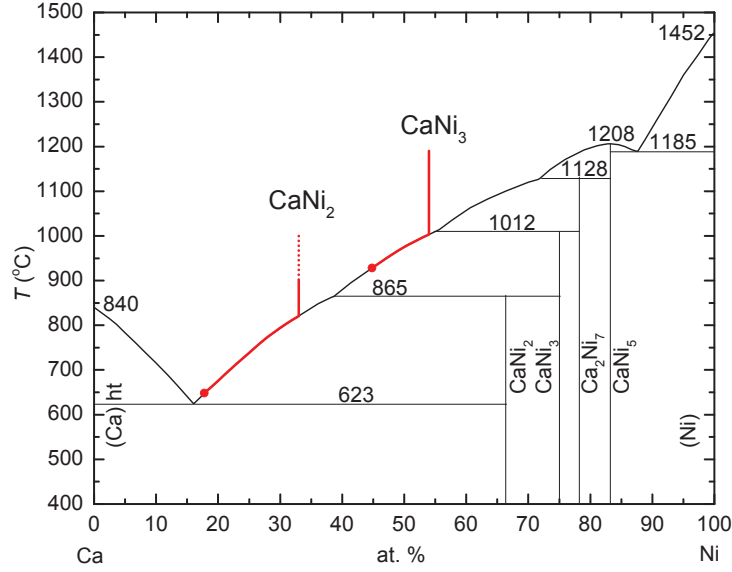
Figure 14: Ca-Ni phase diagram after [34]. Starting compositions, temperature profile and composition of the liquid phase are shown by the red lines (the dotted line represents rapid cooling).

cubic $MgCu_2$ structure type (space group $F\bar{d}3m$) [35]. The lattice parameter was found to be $a = 7.252\,\text{Å}$. $CaNi_3$ crystallizes in the trigonal $PuNi_3$ structure type (space group $R\bar{3}m$) [35]. The lattice parameters were found to be $a = 5.044\,\text{Å}$ and $c = 24.44\,\text{Å}$. Details of the physical measurements and discussion of temperature-dependent magnetization, electrical resistivity, and specific heat have been published separately [36]. The finding of almost itinerant ferromagnetism in these two Ca-based compounds motivated several attempts to tune or modify the magnetic properties by substituting Yb, Y, and La for Ca.

Motivated by the binary phase diagram (Fig. 14) the starting materials for $CaNi_2$ were mixed in a molar ratio of Ca:Ni = 67:33. The mixtures with a total mass of roughly 2.5 g were packed in three-cap Ta crucibles, heated from room temperature to $T = 1000°C$ over 5 h, cooled to 900°C within 1 h, slowly cooled to 650°C over 50 h, and finally decanted. The starting materials for $CaNi_3$ were mixed in a molar ratio of Ca:Ni = 46:54. The mixtures with a total mass of roughly 2.5 g were packed in three-cap Ta crucibles, heated from room temperature to $T = 1190°C$ over 6 h, held for 1/2 h, cooled to 910°C over 32 h and finally decanted. $CaNi_2$ single crystals of octahedral habit with dimensions up to 3 mm were could be obtained (inset Fig. 15). The $CaNi_3$ single crystals show a platelike habit with lateral dimensions of up to 3 mm and a thickness of 0.5 mm (inset Fig. 15).
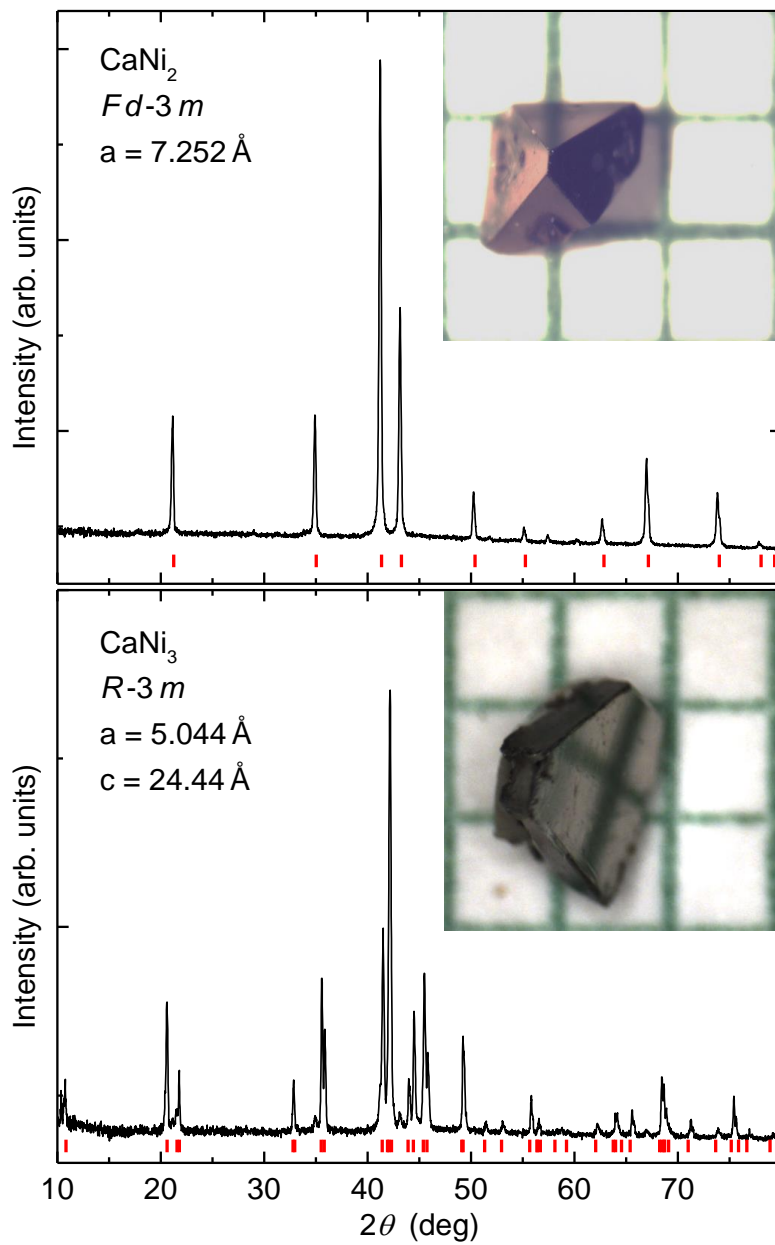
24

Figure 15: X-Ray powder diffraction pattern of CaNi$_2$ and CaNi$_3$ measured on ground single crystals (in air). Representative single crystals are shown on a millimeter grid.

4.2.2 YbNi$_2$

Single crystals of YbNi$_2$ (isostructural to CaNi$_2$) were grown out of a Ca-rich, ternary melt. The starting materials were mixed in a molar ratio of Ca:Yb:Ni = 5:1:2 $\equiv$ Ca$_{62.5}$Yb$_{12.5}$Ni$_{25}$. The mixture with a total mass of roughly 2.5 g was packed in a three-cap Ta crucible, heated from room temperature to $T = 1200°$C over 6 h, held for 0.5 h, slowly cooled to $900°$C over 36 h, and finally decanted. Single crystals of dimensions up to 0.4 mm were obtained. The size of the crystals can be likely increased by optimizing the growth procedure.

Energy dispersive X-Ray analysis, performed on clean, as grown surfaces, indicate a complete absence of Ca in the YbNi$_2$ matrix. This indicates, that, even though CaNi$_2$ and YbNi$_2$ are isostructural, YbNi$_2$ forms out of a Ca melt with no detectable incorporation of Ca. XRD measurements on ground single crystals (Fig. 16a) revealed lattice parameter of $a = 7.092$ Å. This in good agreement with the reported values for YbNi$_2$ ($a = 7.0998(3)$ Å [37], $a = 7.094$ Å [38]) and significantly smaller than the values found for CaNi$_2$ ($a = 7.252$ Å [36]).

Magnetization measurements were performed on clusters of small YbNi$_2$ single crystals. The temperature dependent magnetization data, in Bohr magneton per formula unit (μ_B/f.u.), are shown in Fig. 16b. The magnetization in small applied fields increases step-like upon cooling below $T = 12$ K in accordance with the proposed ferromagnetic ordering [37]. The width of the transition is certainly not larger than in polycrystalline samples (compare with Fig. 2 in [37]) in accordance with good quality samples. Isothermal measurements at $T = 2$ K reveal a strong increase of the magnetization in small applied fields but negligible hysteresis (Fig. 16c). The isothermal magnetization at $T = 2$ K keeps increasing up to the largest applied field of 7 T. A lower limit of 1.5 μ_B/f.u. can be set for the saturation magnetization. Similar field-dependence and magnetization values are observed in polycrystalline material [37]. The temperature-dependent inverse magnetic susceptibility (not shown) follows a Curie-Weiss behavior for $T > 50$ K. The effective moment is found to 4.2(2) μ_B/f.u. in fair agreement with the expectation value for Yb^{3+} (4.54 μ_B). An antiferromagnetic Weiss temperature of $\Theta_W = -13(4)$ K is observed.

4.2.3 Y$_2$Ni$_7$

In order to further explore the potential of Ca-Ni-R (R = rare earth element) melts we shifted to $R = $ Y. An initial melt with the molar ratios Ca : Y : Ni = 41.9 : 4.5 : 53.6 mainly led to the formation of CaNi$_3$ single crystals possibly with some Y substituted for Ca. However, X-Ray powder diffraction pattern, recorded on several batches of crushed single crystals, indicated significant amounts of YNi$_5$ even though the collected single crystals showed a similar habit. If both phases are inter grown within the same single crystal could not be settled unambiguously. Therefore, these results are briefly discussed in section 5. Increasing the Y concentration by a factor of 2 to Ca : Y : Ni = 37.5 : 9.0 : 53.6 led to the formation of Y$_2$Ni$_7$ (Gd$_2$Co$_7$ structure type). An average Ca concentration of 2(1)%, close to the resolution limit, was found by energy dispersive
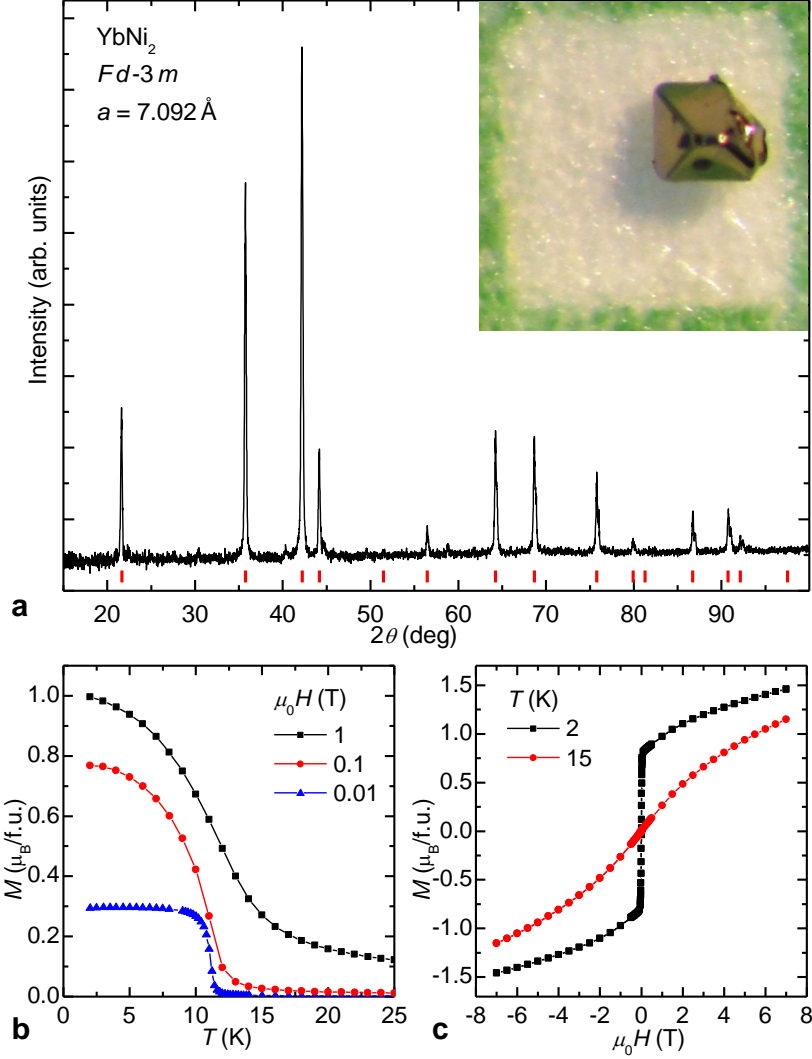
Figure 16: a, X-Ray powder diffraction pattern of YbNi$_2$ (collected in air). The theoretical peak positions are marked by red bars. The inset shows a single crystal of YbNi$_2$ on a millimeter grid. b, The temperature dependent magnetization of YbNi$_2$ increases step-like for cooling below $T = 12\,\mathrm{K}$ indicating ferromagnetic ordering. c, The isothermal magnetization increases rapidly in small applied fields consistent with the proposed ferromagnetic ordering. Polycrystalline samples, synthesized without Ca, show similar behavior [37], indicating the absence of significant amounts of Ca impurities in the flux grown single crystals.
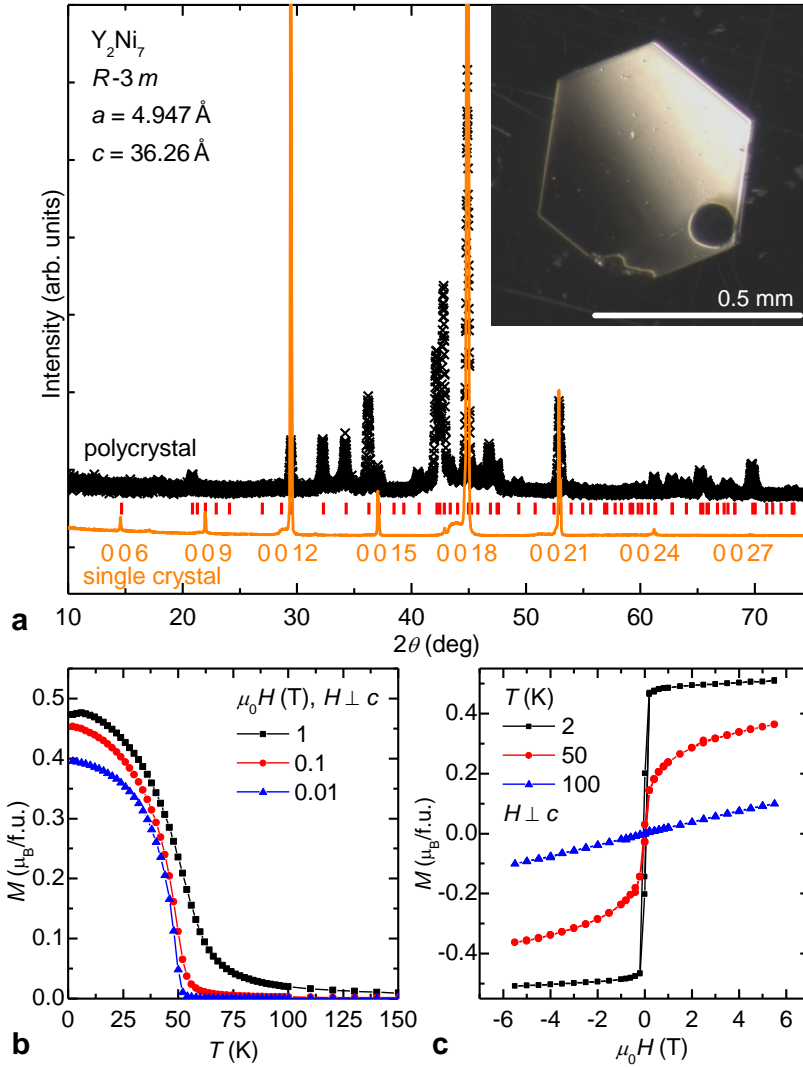
Figure 17: a, X-Ray diffraction pattern of Y_2Ni_7 measured (in air) on ground single crystals (black crosses) and on a single crystal mounted with the plate-like surface laid flat against the sample holder, i.e. with the surface normal of the sample parallel to the scattering vector (solid, orange line). The theoretical peak positions are marked by red bars. The peaks observed for the single crystal can be indexed based on the $0\,0\,3l$ reflections and the obtained c-axis lattice parameters are in good agreement with the literature data. The inset shows a single crystal of Y_2Ni_7 with scale bar. b, The step-like increase in the temperature-dependent magnetization of Y_2Ni_7 for cooling below $T = 55\,\mathrm{K}$ and c, the rapid increase in small applied fields indicate ferromagnetic ordering. Polycrystalline samples, synthesized without Ca, show similar behavior [39], indicating the absence of significant amounts of Ca impurities in the flux grown single crystals.

X-Ray analysis. The mixtures were packed in three-cap Ta crucibles, heated from room temperature to $T = 1190°C$ over 6 h, held for 1/2 h, cooled to T = 910°C over 32 h, and finally decanted to separate the single crystals from the excess flux. We obtained Y_2Ni_7 single crystals with lateral dimensions of up to 0.5 mm and thickness of ~ 0.1 mm (Fig. 17a).

It is worth mentioning that the synthesis of Y_2Ni_7 from an Y-rich self-flux is not possible at temperatures below $1200°C$ and that excludes the use of silica ampules (which protect the Ta crucible). In contrast, single crystal growth from Ca-flux can be performed at temperatures below $1200°C$ and that is of great practical importance for the growth and optimization of this compound. We are not aware of any previous report on the synthesis of single crystalline Y_2Ni_7.

XRD measurements on ground Y_2Ni_7 single crystals (Fig. 17a) revealed lattice parameters of $a = 4.947$ Å, and $c = 36.26$ Å. This in good agreement with the reported values of $a = 4.924$ Å and $c = 36.07$ Å [40] (Gd_2Co_7 structure type). X-Ray diffraction was also performed on single crystals with the surface normal of the plate-like samples parallel to the scattering vector (Fig. 17a). The main peaks in the diffraction pattern can be indexed based on $0\,0\,3l$ reflections as expected for Y_2Ni_7 (according to the reflection conditions for space group $R\bar{3}m$ with hexagonal axes). Under standard laboratory conditions the samples are not air-sensitive on a timescale of one year.

The temperature dependent magnetization of Y_2Ni_7 increases strongly upon cooling below $T = 55$ K (Fig. 17b), in accordance with the reported ferromagnetic ordering observed in polycrystalline samples [39]. The onset and the temperature dependence of the increase are very similar to the behavior of polycrystalline Y_2Ni_7 (compare with Figs. 1 and 2 in [39] and [41, 42]). Isothermal magnetization measurements at $T = 2$ K reveal a strong increase and fast saturation of the magnetization at $0.51\,\mu_B$/f.u. (Fig. 17c) corresponding to $0.07(1)\,\mu_B$/Ni in good agreement with the reported value ($0.08\,\mu_B$/Ni). The rather small saturation moment is in accordance with the decrease of the saturation moment with decreasing Curie temperature as observed in many Ni-based metallic compounds [39]. Furthermore, it has been reported that the size of the ordered moment in Y_2Ni_7 significantly dependents on Ni vacancies [43]. The moment was found to increase linearly from $0.033\,\mu_B$/Ni in Y_2Ni_7 to $0.083\,\mu_B$/Ni in $Y_2Ni_{6.7}$. Considering these results, albeit obtained on polycrystalline material, a slight Ni deficiency might be inferred for the single crystals reported here.

The similarities to polycrystalline samples, which were synthesized by arc melting and annealing of Y and Ni [39], indicates a negligible effect of possible Ca contaminations or substitutions on the magnetic properties of Y_2Ni_7 or, more likely, the absence of Ca in the single crystals. Similar to the case of $YbNi_2$, the replacement of Ca by a rare earth element seams to be energetically highly favorable in these crystal structures as soon as the rare earth concentration in the melt exceeds a certain threshold. This is even more surprising considering the similar lattice parameters of Ca_2Ni_7 [35] and Y_2Ni_7 [39] with $\Delta a/a = 1.2\%$ and $\Delta c/c = -0.3\%$ ($\Delta a = a_{Ca} - a_Y$ and $\Delta c = c_{Ca} - c_Y$). The different valence states, predominantly Ca^{2+} vs. Y^{3+}, are likely the dominating factor for the observed phase formation.

4.2.4 LaNi$_5$

Exploration of the Ca-Ni-La ternary melt lead to the growth of LaNi$_5$. An initial melt with the molar ratios $Ca:La:Ni = 41.9:4.5:53.6$ led to the formation of LaNi$_5$. The elements were packed in three-cap Ta crucibles, heated from room temperature to $T = 1190°C$ over 6 h, held for 1/2 h, cooled to $T = 910°C$ over 32 h, and finally decanted to separate the single crystals from the excess flux. The LaNi$_5$ single crystals had an isometric habit (in accordance with a rather small c/a ratio) with typical dimensions of 1 mm. Laue-back-reflection pattern show the six-fold rotation symmetry along the crystallographic c-direction (Fig. 18b). XRD measurements on ground LaNi$_5$ single crystals (Fig. 18c) revealed lattice parameters of $a = 5.017$ Å and $c = 3.978$ Å. This is in good agreement with the reported values of $a = 5.013$ Å and $c = 3.984$ Å [44]. An average Ca concentration of 2(1) at.%, close to the resolution limit, was found by energy dispersive X-Ray analysis. Increasing the La concentration by a factor of 2 to $Ca:La:Ni = 37.5:9.0:53.6$ led to the formation LaNi$_x$ with $x \approx 4$ possibly with some Ca substituted for La. However, we found no unique solution to index the X-Ray powder diffraction pattern based on one structure. Therefore, these results are briefly discussed in section 5.

The magnetic susceptibility at room temperature was found to be $\chi = 26 \cdot 10^{-9}$ m^{3}mol^{-1} ($H \parallel c$, $\mu_0 H = 1$ T) in good agreement with the reported value of $\chi = 23 \cdot 10^{-9}$ m^{3}mol^{-1} obtained on polycrystalline material [45]. $\chi(T)$ shows a roughly linear increase by $\sim 20\%$ upon cooling to $T = 20$ K (inset Fig. 18c). A similar increase was also observed in polycrystalline material for cooling down to ~ 100 K [45]. A further, enhanced increase upon cooling below ~ 20 K (Curie tail) can be attributed to a small amount of local moment bearing magnetic impurities.

5 Ambiguous and failed attempts

In addition to the crystal growths detailed above, there have been growth attempts that have led to either ambiguous phases or failure to yield sufficiently large samples by the decanting temperature. The classification of the results as being ambiguous or failed is by no means meant to be a final statement. Very small changes in the composition of the ternary, quaternary or quinary melts and/or variations in the temperature profile can have dramatic effects on the phase formation. The intention is rather to give a comprehensive overview of growth attempts for which the result was:

- dramatically different from the goal of the synthesis,

- not identifiable,

- a total spin (decanting above the liquidus temperature),

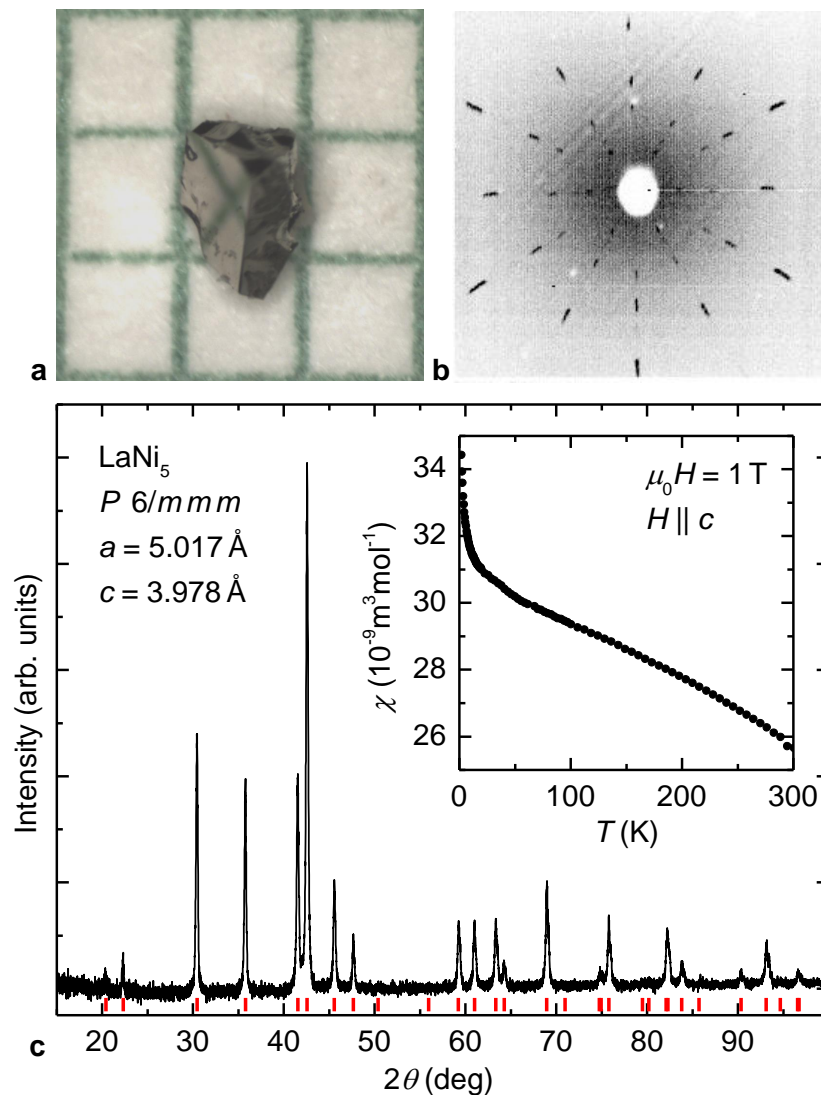- polycrystalline material which can be easily obtained else-wise.

Figure 18: a, LaNi$_5$ single crystal on a millimeter grid and b, corresponding Laue-back-reflection pattern. c, X-Ray powder diffraction pattern of LaNi$_5$ measured on ground single crystals (in air). The theoretical peak positions for the reported structure are marked by red bars. The inset shows the temperature-dependent magnetic susceptibility $\chi = M/H$.
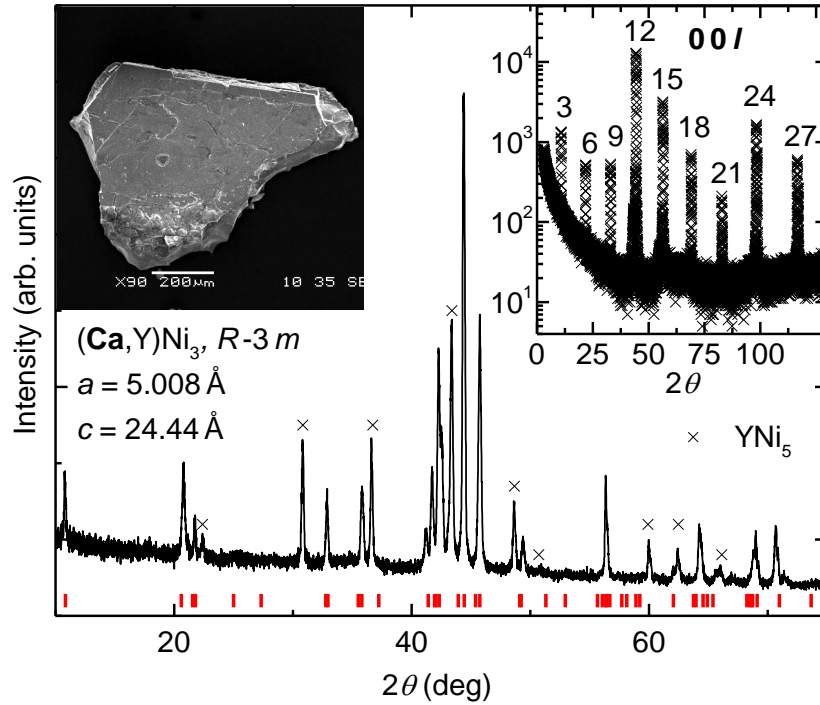
Figure 19: X-Ray powder diffraction pattern of $(\mathbf{Ca},Y)Ni_3$ measured on ground single crystals (in air). An electron micrograph of an as-grown sample is shown as inset to the left. The right hand inset shows the diffraction pattern obtained on this single crystal which was mounted with the plate-like surface laid flat against the sample holder, i.e. with the surface normal of the sample parallel to the scattering vector. The peaks observed for the single crystal can be indexed based on the $0\,0\,3l$ reflections and the obtained c-axis lattice parameters are in good agreement with the literature data (the number given in the plot is the l Miller index).

These growths include attempts to incorporate Ag, As, Au, B, Cr, Cu, Mg, Sc, Tb, Ti, and V into Li or Ca based melts. Two compounds, $(\mathbf{Ca},Y)Ni_3$ and $LaNi_x$, are presented in more detail at the beginning of this section whereas the other growth attempts are briefly described in tabular form below (Tab. 1).

$(\mathbf{Ca},Y)Ni_3$: An initial melt with the molar ratios $Ca : Y : Ni = 41.9 : 4.5 : 53.6$ led to the formation of $CaNi_3$ possibly with some Y substituted for Ca. Energy dispersive X-Ray analysis on four samples (on 17 spots in total) revealed an Y concentration of $4(1)$ at.% and a Ca concentration of $22(4)$ at.% corresponding to $(Ca_{0.85}Y_{0.15})Ni_3$. Due to the large uncertainty in the Y concentration, the compound is denoted as $(\mathbf{Ca},Y)Ni_3$. The mixtures were packed in three-cap Ta crucibles, heated from room temperature to $T = 1190°C$ over $6\,h$, held for $1/2\,h$, cooled to $T = 910°C$ over $32\,h$, and finally decanted to separate the single
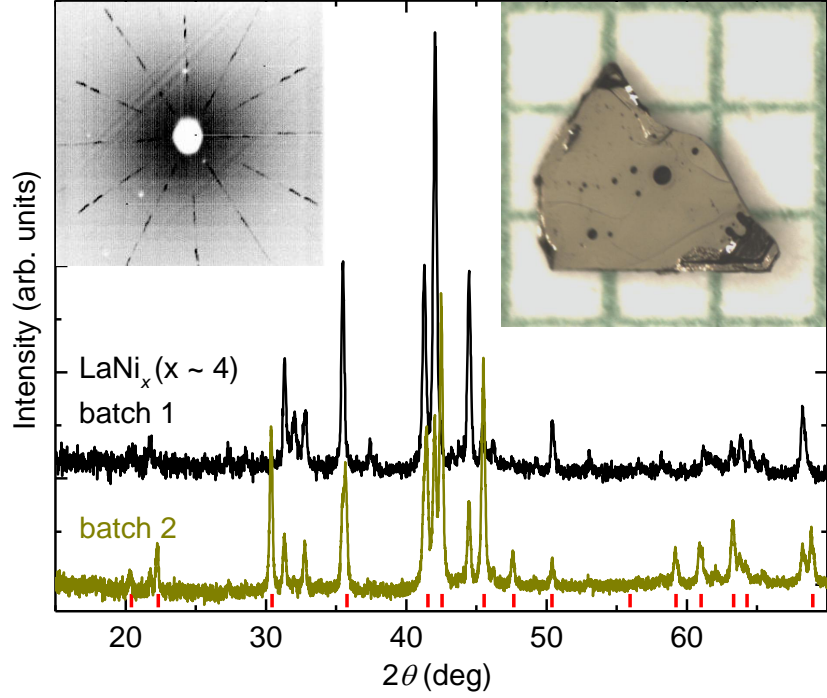
Figure 20: Two X-Ray diffraction pattern of $LaNi_x$ measured on ground single crystals (in air). The theoretical peak positions for $LaNi_5$ are shown by red bars. The right hand inset shows an as-grown single crystal. A corresponding Laue-back-reflection pattern is shown as inset to the left.

crystals from the excess flux. We obtained single crystals with lateral dimensions of up to $1\,mm$ and thickness of $\sim 0.2\,mm$ for $(\mathbf{Ca},Y)Ni_3$ (inset Fig. 19). XRD measurements on ground single crystals (Fig. 19) can be indexed assuming a mixture of $(\mathbf{Ca},Y)Ni_3$ and $(Ca,Y)Ni_5$. However, we can not exclude the presence of a possible superstructure [46]. The $(\mathbf{Ca},Y)Ni_3$ lattice parameters of $a = 5.008\,Å$, and $c = 24.44\,Å$ are close to the values of $a = 5.044\,Å$ and $c = 24.44\,Å$ that were found in undoped $CaNi_3$ which was synthesized by the same growth procedure [36]. X-Ray diffraction was also performed on single crystals with the surface normal of the plate-like samples parallel to the scattering vector (inset Fig. 19, the given number is the Miller index l). All peaks in the diffraction pattern can be indexed based on $0\,0\,3l$ reflections as expected for $CaNi_3$ (according to the reflection conditions for space group $R\bar{3}m$ with hexagonal axes).

The magnetic properties of $(\mathbf{Ca},Y)Ni_3$ are indistinguishable from pure $CaNi_3$ [36] within the error of the measurements.

$LaNi_x$: An initial melt with the molar ratios $Ca:La:Ni = 37.5:9.0:53.6$ led to the formation of single crystalline $LaNi_x$ with $x \approx 4$ possibly with some Ca

substituted for La. We obtained plate-like single crystals with lateral dimensions of up to $2\,\mathrm{mm}$ and thickness of $\sim 0.4\,\mathrm{mm}$ (Fig. 20). Ca concentrations of $3(1)\,\mathrm{at.\%}$ and Ni concentrations of $\sim 80\,\mathrm{at.\%}$ were estimated by energy dispersive X-Ray analysis. The majority of X-Ray powder diffraction peaks can be indexed based on the structure of $LaNi_3$ or La_5Ni_{19}. However, the solution is not unique and additional peaks appear. A measurement on a second batch of ground single crystals also indicated the presence of a significant amount of $LaNi_5$. Furthermore, X-Ray diffraction on single crystal with the surface normal of the plate-like samples parallel to the scattering vector showed well defined Bragg peaks at low angles indicating a periodicity of $50\,\text{Å}$ along the c-axis. It is known that several La-Ni compounds can be considered as varying stacking sequence build from La_2Ni_4 and $LaNi_5$ block layers [47]. In fact, long-range superstructures with periodicities of $49\,\text{Å}$ and above along the c-axis have been found in La-Mg-Ni based alloys [46]. Therefore, the formation of superstructures in Ca-substituted $LaNi_x$ and in $(\mathbf{Ca},\mathrm{Y})Ni_3$ seem not unlikely. However, a further investigation of this possibility is beyond the scope of this publication.

Further growth attempts are summarized in Tab. 1. The goal of the growth is given in column one followed by the molar ratio of the starting materials in column two. The temperature profile is given in column three where the first number denotes the time in hours to reach the first temperature set point (starting from between room-temperature and $\sim 200^\circ\mathrm{C}$). The last number gives the decanting temperature. Column four describes the results of the growths.

6 Summary

We demonstrate the use of Li and Ca flux for the single crystal growth of various compounds. The synthesis of large nitride single crystals from Li- or Ca-rich flux is, to our knowledge, demonstrated for the first time and has several advantages compared to the more common reactions from the elements with N_2 gas.

Growth attempts for several Li-transition metal binaries are reported and we present a basic, physical characterization of LiRh as well as magnetic properties of Li_2Pd, Li_2Pt, Li_3Al_2, $YbNi_2$, Y_2Ni_7, and $LaNi_5$. A surprising discovery was the successful growth of single crystalline rare earth-nickel binaries from Ca flux that were essentially free from Ca incorporations.

The viability of Li and Ca flux is by no means meant to be restricted to the presented compounds. Rather, we hope to have demonstrated the wide range of applications these elements can have for growing various compounds and provide practical, technical solutions to overcome the difficulties associated with the high reactivity of Li and Ca.

Table 1: Ambiguous and failed growth attempts

Goal	Initial composition	Temperature profile (°C)	Result
$Ag_{16}Ca_6N$	Ca:Ag:Ca$_3$N$_2$ = 33:32:1	5h-1180-0.5h-1180-24h-900	total spin
$Ag_8Ca_{19}N_7$	" = 131:16:7	"	Ca$_2$N, brittle Ta
$AlLi_3N_2$	Li:Al:Li$_3$N=11:1:2	4h-900-44h-400	small amount of AlN poly
"	=10:2:2	"	AlN poly
BN	Cu:Li:Li$_3$N:B=87: 48:13:13	6h-1200-1h-1200-60h-900	Li$_3$BN$_2$, Cu$_3$N, unidentified transparent flakes
"	Pd:Li:Li$_3$N:B=67:144:39:33	"	Li$_3$BN$_2$, Li$_2$Pd
Ca_3AuN	Ca:Au:Ca$_3$N$_2$=21:2:1	6h-1200-0.3h-1200-36h-900	total spin
"	=21:2:1	5.5h-1100-1.5h-920-40h-825	Ca$_2$N
"	=15:2:3	"	"
"	=33:2:1	6h-1200-32h-880	"
$CaMg_2N_2$	Ca:Mg:Ca$_3$N$_2$=82.5:5:2.5	4h-940-1h-940-50h-840	Ca$_2$N SC
CaNiN	Ca:Ni:Ca$_3$N$_2$ = 5:4:1	5 h-1000-1 h-900-50 h-650	Ca$_2$N SC
"	= 9:4:1	"	"
"	= 13:6:1	"	"
"	= 17:8:1	"	"
CeFeAsO	Ca:Ce:Fe:As:Fe$_2$O$_3$=60:3:1:3:1	6h-1200-0.5h-1200-40-880	Ce$_4$As$_3$ SC
$CeLi_2N_2$	Li:Ce:Li$_3$N=5.5:0.5:1	4.5h-900-1.5h-750-44h-350	Li$_3$N SC, Ce
$LiAgC_2$	Li:Ag:C=18:1:2	5h-1000-1h-1000-60h-400	Li$_2$C$_2$ SC + AgLi poly
"	=18:2:2	"	"
LiFeAs	Li:FeAs:As=4:1:1	6h-850-50h-550	LiFeAs poly
"	"	9h-950-50h-550	"
"	"	11h-1050-50h-750	"
LiMgN	Li:Mg:Li$_3$N=5:1:1	4.5h-900-1.5h-750-100h-350	Li$_3$N SC
$Li_2(Li_{0.7}Sc_{0.3})N$	Li:Sc:Li$_3$N=5.7:0.3:1	4.5h-900-1.5h-750-100h-350	Li$_3$N SC
$Li_2(Li_{0.7}Ti_{0.3})N$	Li:Ti:Li$_3$N= "	"	"
$Li_2(Li_{0.7}V_{0.3})N$	Li:V :Li$_3$N= "	"	"
$Li_2(Li_{0.7}Cr_{0.3})N$	Li:Cr:Li$_3$N= "	"	"
Li_2Pt_3B	Li:Pt:B=9:3:1	4h-1000-1h-1000-20h-700	total spin
"	"	4h-1000-1h-1000-1.5h-720-20h-500	Li$_2$Pt
"	Li:Pt:B=69:15:16	4h-700-4h-700-40h-500	unidentified SC, isometric habit
Li_2Pd_3B	Li:Pd:B=69:15:15	"	unidentified crystalline material, needle-like habit
$TbCu_2$	Li:Tb:Cu=92.5:2.5:5	4h-900-47h-400	TbCu$_2$ poly
"	=85.0:5.0:10	"	"

Crucible material: Ta. Temperature profile: the first number denotes the time (in hours) to reach the first temperature which is given by the second number in °C, the third number denotes the time to reach the next temperature, which is given by number 4, etc. Abbreviations: SC = single crystal, poly = polycrystalline

References

[1] Canfield, P. C. & Fisher, I. R. High-temperature solution growth of inter-metallic single crystals and quasicrystals. *J. Cryst. Growth* **225**, 155–161 (2001).

[2] Larson, A. C. & Von Dreele, R. B. "General Structure Analysis System (GSAS)", Los Alamos National Laboratory Report LAUR 86-748 (2000).

[3] Toby, B. H. EXPGUI, a graphical user interface for GSAS. *J. Appl. Crystallogr.* **34**, 210–213 (2001).

[4] Honig, R. E. & Kramer, D. A. Vapor Pressure Data for the Solid and Liquid Elements. *RCA Review* **30**, 285–305 (1969).

[5] Lyublinski, I. E., Evtikhin, V. A., Pankratov, V. Y. & Krasin, V. P. Numerical and experimental determination of metallic solubilities in liquid lithium, lithium-containing nonmetallic impurities, lead and lead-lithium eutectic. *J. Nucl. Mater.* **224**, 288–292 (1995).

[6] Sangster, J. & Pelton, A. D. Li-Pd Phase Diagram, ASM Alloy Phase Diagrams Center, P. Villars, editor-in-chief; H. Okamoto and K. Cenzual, section editors; http://www1.asminternational.org/AsmEnterprise/APD, ASM International, Materials Park, OH, 1990.

[7] Sangster, J. & Pelton, A. D. Li-Pt Phase Diagram, ASM Alloy Phase Diagrams Center, P. Villars, editor-in-chief; H. Okamoto and K. Cenzual, section editors; http://www1.asminternational.org/AsmEnterprise/APD, ASM International, Materials Park, OH, 1990.

[8] Kanatzidis, M. G., Pöttgen, R. & Jeitschko, W. The metal flux: A preparative tool for the exploration of intermetallic compounds. *Angew. Chem. Int. Ed.* **44**, 6996–7023 (2005).

[9] Okamoto, H. Li-N Phase Diagram, ASM Alloy Phase Diagrams Center, P. Villars, editor-in-chief; H. Okamoto and K. Cenzual, section editors; http://www1.asminternational.org/AsmEnterprise/APD, ASM International, Materials Park, OH, 1990.

[10] Rabenau, A. & Schulz, H. Re-evaluation of the lithium nitride structure. *J. Less-Common Met.* **50**, 155 – 159 (1976).

[11] Sachsze, W. & Juza, R. Metallamide und Metallnitride, 21. Mitteilung. Über Mischkristalle der Zusammensetzung $(Li, Co)_3N$, $(Li, Ni)_3N$ und $(Li, Cu)_3N$. *Z. Anorg. Chem.* **259**, 278–290 (1949).

[12] Jesche, A. *et al.* Giant magnetic anisotropy and tunnelling of the magnetization in $Li_2(Li_{1-x}Fe_x)N$. *Nat. Commun.* 5:3333 doi: 10.1038/ncomms4333 (2014).

[13] Niewa, R., Huang, Z. L., Schnelle, W., Hu, Z. & Kniep, R. Preparation, Crystallographic, Spectroscopic and Magnetic Characterization of Low-Valency Nitridometalates Li2[(Li$_{1-x}$M$_x$)N] with M = Cu, Ni. *Z. Anorg. Allg. Chem.* **629**, 1778–1786 (2003).

[14] Yim, W. M. & Paff, R. J. Thermal expansion of aln, sapphire, and silicon. *J. Appl. Phys.* **45**, 1456–1457 (1974).

[15] Cordier, G., Gudat, A., Kniep, R. & Rabenau, A. LiCaN und Li$_4$SrN$_2$, Abkömmlinge der Fluorit- bzw. Lithiumnitrid-Struktur. *Angew. Chem.* **101**, 1689–1695 (1989).

[16] Juza, R. & Wehle, V. Kristallstruktur des Lithiumcarbids. *Naturwissenschaften* **52**, 537–537 (1965).

[17] Ruschewitz, U. & Pöttgen, R. Structural Phase Transition in Li$_2$C$_2$. *Z. Anorg. Allg. Chem.* **625**, 1599–1603 (1999).

[18] Hallstedt, B. & Kim, O. Al-Li Phase Diagram (calculated), ASM Alloy Phase Diagrams Center, P. Villars, editor-in-chief; H. Okamoto and K. Cenzual, section editors; http://www1.asminternational.org/AsmEnterprise/APD, ASM International, Materials Park, OH, 2007.

[19] Tebbe, K. F., Schnerin, H. G., Ruter, B. & Rabeneck, G. LI$_3$AL$_2$, a new phase in the system Li−Al. *Z. Naturforsch., B: Chem. Sci.* **B-28**, 600–605 (1973).

[20] van Vucht, J. H. N. & Buschow, K. H. J. Note on the occurrence of intermetallic compounds in the lithium-palladium system. *J. Less-Common Met.* **48**, 345–347 (1976).

[21] Bronger, W., Nacken, B. & Ploog, K. Zur synthese und struktur von Li$_2$Pt und LiPt. *J. Less-Common Met.* **43**, 143–146 (1975).

[22] Lee, C., Whangbo, M.-H. & Köhler, J. Analysis of electronic structures and chemical bonding of metal-rich compounds. I. Density functional study of Pt metal, LiPt$_2$, LiPt, and Li$_2$Pt. *J. Comput. Chem.* **29**, 2154–2160 (2008).

[23] Massalski, T. B. (ed.) *Binary Alloy Phase Diagrams*, vol. 3 (William W. Scott, 1990).

[24] Sidhu, S. S., Anderson, K. D. & Zauberis, D. D. Neutron and X-ray diffraction study of LiRh. *Acta Cryst.* **18**, 906–907 (1965).

[25] Cenzual, K., Gelato, L. M., Penzo, M. & Parthé, E. Inorganic structure types with revised space groups. I. *Acta Crystallogr., Sect. B: Struct. Sci.* **47**, 433–439 (1991).

[26] Donkersloot, H. C. & van Vucht, J. H. N. The crystal structure of IrLi, Ir$_3$Li and LiRh$_3$. *J. Less-Common Met.* **50**, 279–282 (1976).

[27] Magee, C. B. A study of the synthesis and properties of the transition-metal hydryls, Final Report to the Joint US/EURATOM Research and Development Program, Contract No. AT(ll-l)-1185, Denver Research Institute, University of Denver, EURAEC 1251 (DRI 2189), October 1964.

[28] Varma, S. K., Chang, F. C. & Magee, C. B. Compounds and phase relationships in the lithiumiridium-hydrogen system. *J. Less-Common Met.* **60**, P47–P63 (1978).

[29] Simon, S. H. *The Oxford solid state basics, p. 13* (Oxford University Press, Oxford, United Kingdom, 2013).

[30] ASM Alloy Phase Diagrams Center, http://www1.asminternational.org/asmenterprise/APD/default.aspx.

[31] Itkin, V. P. & Alcock, C. B. Ca-N Phase Diagram, ASM Alloy Phase Diagrams Center, P. Villars, editor-in-chief; H. Okamoto and K. Cenzual, section editors; http://www1.asminternational.org/AsmEnterprise/APD, ASM International, Materials Park, OH, 1990.

[32] Höhn, P. *et al.* β-Ca_3N_2, a Metastable Nitride in the System Ca-N. *Chem. Eur. J.* **15**, 3419–3425 (2009).

[33] Gregory, D. H., Bowman, A., Baker, C. F. & Weston, D. P. Dicalcium nitride, Ca_2N - a 2D 'excess electron' compound; synthetic routes and crystal chemistry. *J. Mater. Chem.* **10**, 1635–1641 (2000).

[34] Okamoto, H. Ca-Ni Phase Diagram, ASM Alloy Phase Diagrams Center, P. Villars, editor-in-chief; H. Okamoto and K. Cenzual, section editors; http://www1.asminternational.org/AsmEnterprise/APD, ASM International, Materials Park, OH, 1990.

[35] Buschow, K. H. J. Calcium-nickel intermetallic compounds. *J. Less-Common Met.* **38**, 95–98 (1974).

[36] Jesche, A., Dennis, K. W., Kreyssig, A. & Canfield, P. C. Nearly itinerant ferromagnetism in $CaNi_2$ and $CaNi_3$. *Phys. Rev. B* **85**, 224432 (2012).

[37] Rojas, D. P., Fernández Barquín, L., Echevarria-Bonet, C. & Rodríguez Fernández, J. $YbNi_2$: A heavy fermion ferromagnet. *Solid State Commun.* **152**, 1834–1837 (2012).

[38] Buschow, K. H. J. Note on the structure and occurrence of ytterbium transition metal compounds. *J. Less-Common Met.* **26**, 329–333 (1972).

[39] Buschow, K. H. J. Magnetic properties of Y_2Ni_7 and its hydride. *J. Less-Common Met.* **97**, 185–190 (1984).

[40] Virkar, A. V. & Raman, A. Crystal structures of AB_3 and A_2B_7 rare earth-nickel phases. *J. Less-Common Met.* **18**, 59–66 (1969).

[41] Nishihara, Y. & Ogawa, S. Itinerant Electron Ferromagnetism in Y_2Ni_7 and Mössbauer Effect of ^{57}Fe Doped in Y_2Ni_7. *J. Phys. Soc. Jpn.* **60**, 300–303 (1991).

[42] Bhattacharyya, A., Jain, D., Ganesan, V., Giri, S. & Majumdar, S. Investigation of weak itinerant ferromagnetism and critical behavior of Y_2Ni_7. *Phys. Rev. B* **84**, 184414 (2011).

[43] Nakabayashi, R., Tazuke, Y. & Murayama, S. Itinerant Electron Weak Ferromagnetism in Y_2Ni_7 and YNi_3. *J. Phys. Soc. Jpn.* **61**, 774–777 (1992).

[44] Wernick, J. H. & Geller, S. Transition element−Rare Earth Compounds with $CuSb_5Ca$ Structure. *Acta Cryst.* **12**, 662–665 (1959).

[45] Burzo, E., Chiuzbăian, S. G., Chioncel, L. & Neumann, M. Magnetic and electronic properties of the $LaNi_{5-x}Cu_x$ system. *J. Phys. Condens. Matter* **12**, 5897 (2000).

[46] Ozaki, T. *et al.* Stacking structures and electrode performances of rare earth−Mg−Ni-based alloys for advanced nickel−metal hydride battery. *J. Less-Common Met.* **446-447**, 620–624 (2007).

[47] Yamamoto, T. *et al.* Microstructures and hydrogen absorption/desorption properties of La−Ni alloys in the composition range of La−77.8 ∼ 83.2 at. % Ni. *Acta Mater.* **45**, 5213–5221 (1997).